Supporting Information for "Insights into Deep Mantle Thermochemical Contributions to African Magmatism from Converted Seismic Phases"

A. Boyce[1], S. Cottaar[1]

[1]University of Cambridge, Department of Earth Science, Bullard Laboratories, Madingley Road,

Cambridge, CB3 0EZ, UK.

Contents of this file

Corresponding author: Alistair Boyce, `ab2568@cam.ac.uk`

1 Introduction

The file *Boyce_and_Cottaar_Africa_RFs_MTZ_depths.txt* distributed as a supplement with this manuscript provides a text file of the picked MTZ discontinuity depths below Africa obtained from this study. Values are obtained from AFRP20-CCP combining Pds, PPds, PKPds data corrected to depth using the 3D tomographic model AFRP20 (Boyce et al., 2021). RFs are calculated up to a maximum frequency of 0.2 Hz. Values are only provided for regions where stacking weight (Figure S6) and standard error are greater than two.

2 Epicentral Distance Stacks

Figures S1–S3 show epicentral distance stacks for Pds, PPds and PKPds data sets that contribute to CCP stacks in the main manuscript. Each plot shows clear P410s and P660s arrivals and the distance ranges that were removed due to interfering phases.
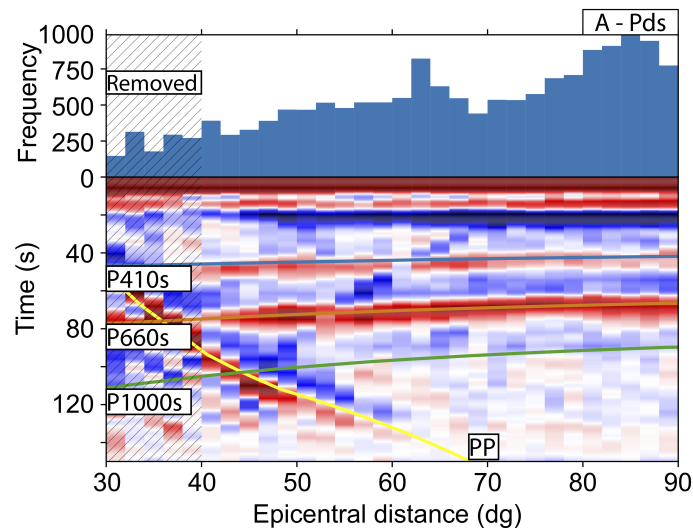

Figure S1. Receiver function stacks (data pre-filtered at 0.01–0.2 Hz) binned by epicentral distance for 16430 Pds RFs. Predicted moveout of converted phases are labeled. "Removed" epicentral distance bins are excluded from subsequent CCP stacking to limit interference of other phases/multiples with converted arrivals from the mantle transition zone.

Figure S2. Receiver function stacks (data pre-filtered at 0.01–0.2 Hz) binned by epicentral distance for 13678 PPds RFs. Predicted moveout of converted phases are labeled. "Removed" epicentral distance bins are excluded from subsequent CCP stacking to limit interference of other phases/multiples with converted arrivals from the mantle transition zone.
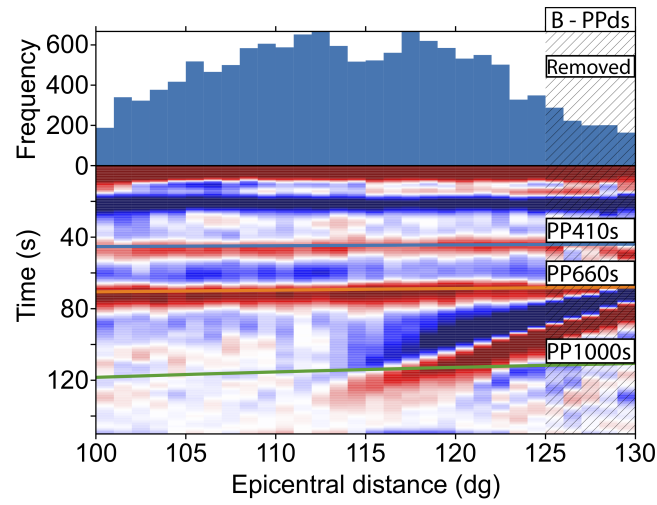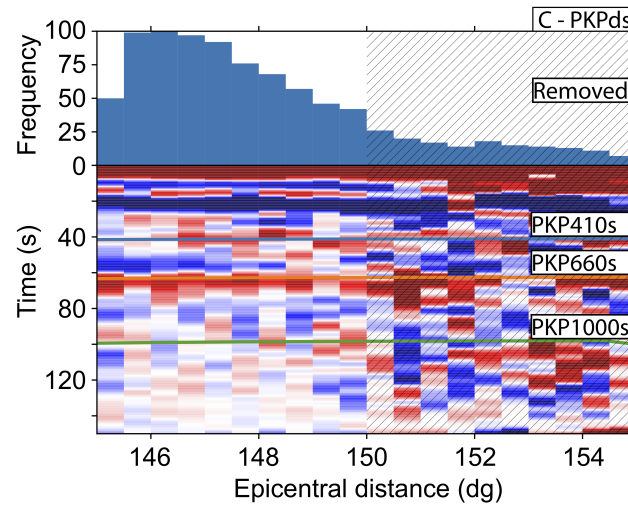

Figure S3. Receiver function stacks (data pre-filtered at 0.01–0.2 Hz) binned by epicentral distance for 885 PKPds RFs. Predicted moveout of converted phases are labeled. "Removed" epicentral distance bins are excluded from subsequent CCP stacking since strong converted phases are lacking from the higher epicentral distances likely due to steep incidence angles at mantle transition zone discontinuities.

3 Regional MTZ Depth and Slowness Stacks

Figures S4–S5 show depth and slowness stacks for RFs whose piercing points at 410 km depth fall within the given region. Depth stacks comprise RFs corrected to depth using the AFRP20 tomographic model (Boyce et al., 2021). Regions are shown in map view on Figure 2 of the main manuscript and Table S1. Outwith the d410 below CAM, all regions show clear conversions from the d410 and d660 at the expected slowness. Only SAF shows a confident observation of the multiple from the d410. Only EAR shows a clear arrival from ∼1000 km at the expected slowness.
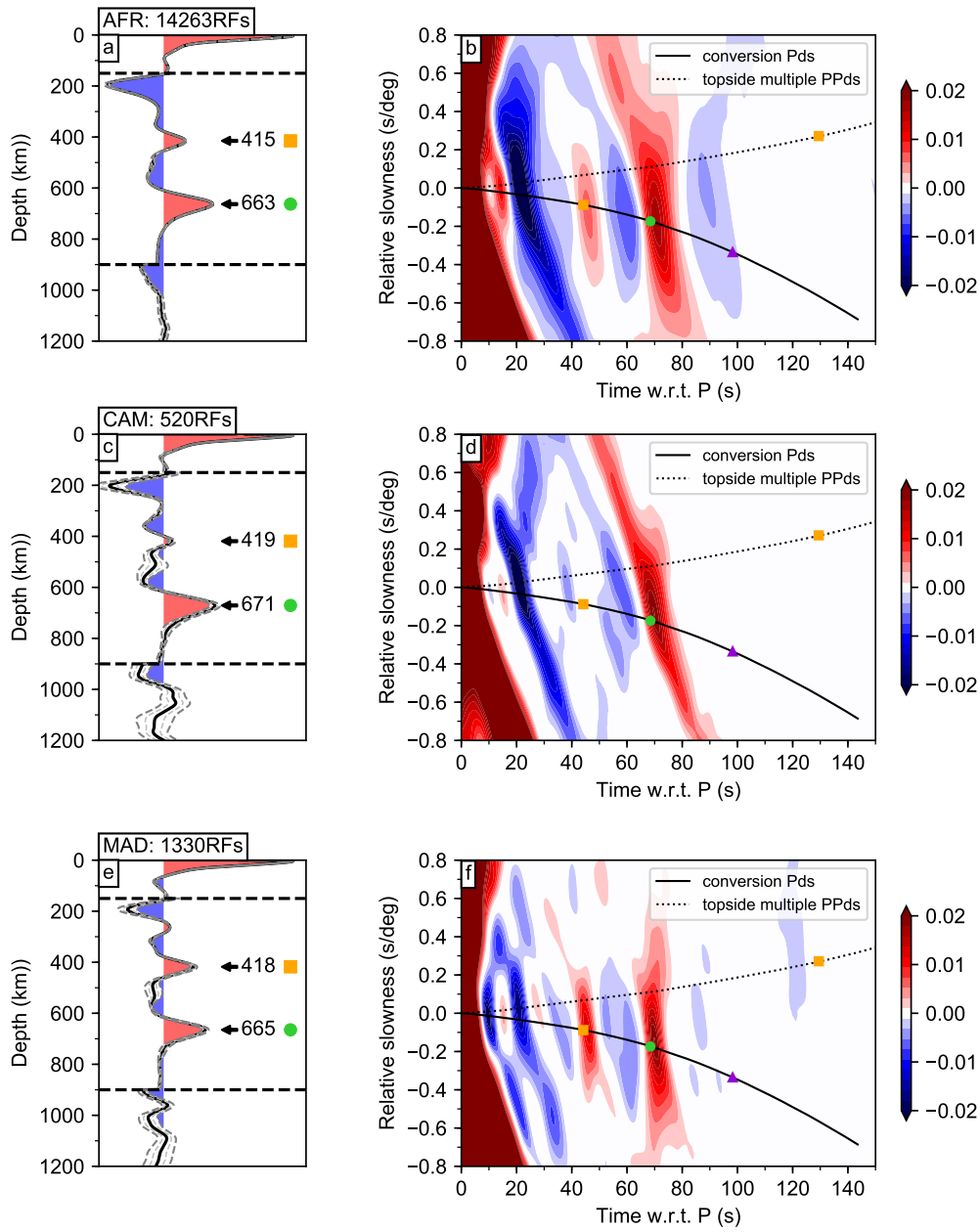
Figure S4. Regional depth (*a,c,e*) and slowness stacks (*b,d,f*) for Pds data whose piercing points at 410 km depth fall within in the specified regions: AFR, CAM, MAD. Regions are defined in Table S1. RF max frequency is 0.2 Hz. Depth stacks comprise RFs corrected to depth using the AFRP20 tomographic model (Boyce et al., 2021). The depth of high amplitude positive peaks at MTZ depths are labeled. Depth stack amplitudes are multiplied by five and twenty below 150 km and 900 km respectively. Predicted converted Pds arrivals have negative slowness (solid line), multiples have positive slowness (dashed line) w.r.t. direct-P phase. Orange square: d410 conversion/multiple. Green circle: d660 conversion/multiple. Violet triangle: d1000 conversion/multiple.
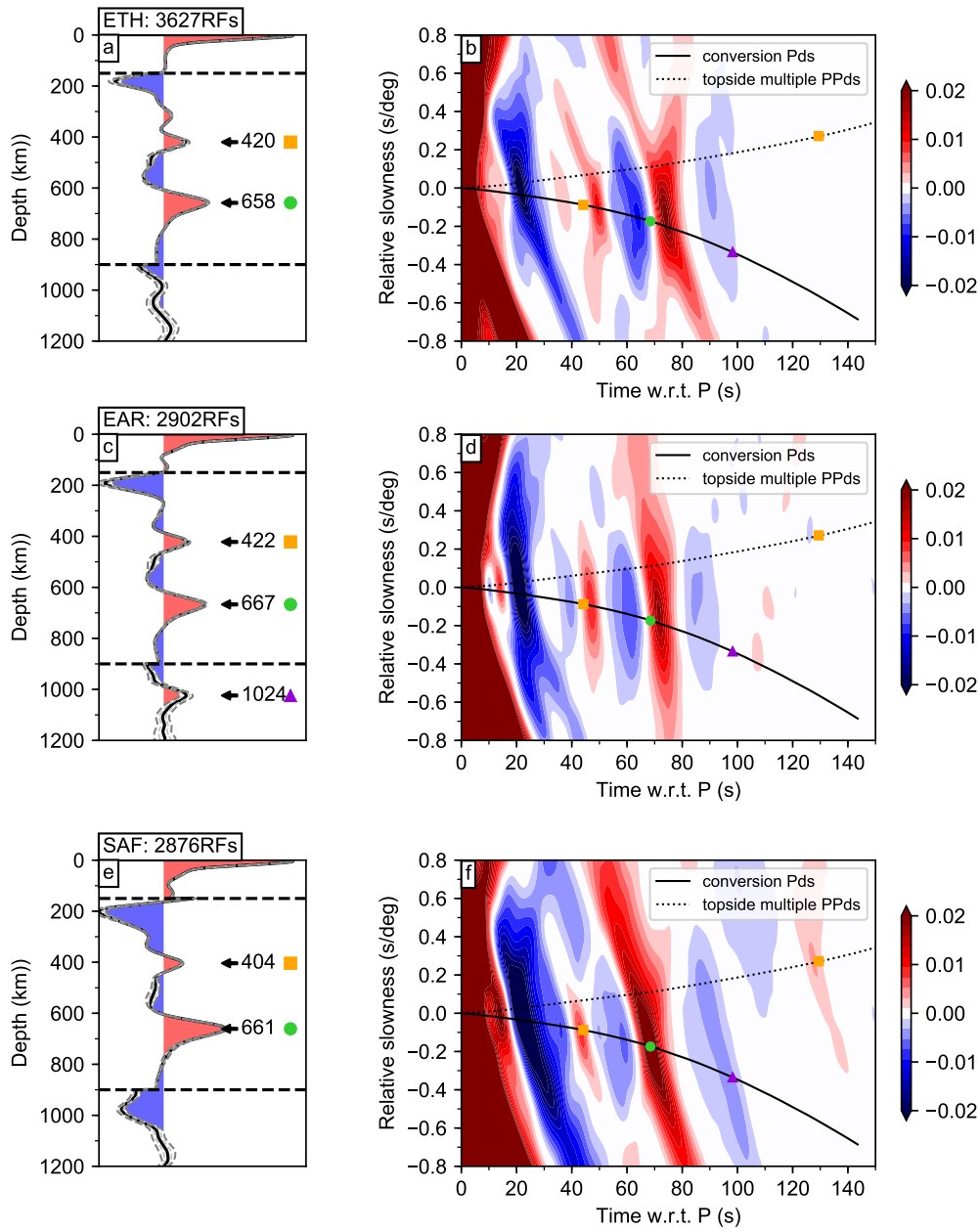
Figure S5. Regional depth (*a,c,e*) and slowness stacks (*b,d,f*) for Pds data whose piercing points at 410 km depth fall within in the specified regions: ETH, EAR, SAF. Regions are defined in Table S1. RF max frequency is 0.2 Hz. Depth stacks comprise RFs corrected to depth using the AFRP20 tomographic model (Boyce et al., 2021). The depth of high amplitude positive peaks at and below MTZ depths are labeled. Depth stack amplitudes are multiplied by five and twenty below 150 km and 900 km respectively. Predicted converted Pds arrivals have negative slowness (solid line), multiples have positive slowness (dashed line) w.r.t. direct-P phase. Orange square: d410 conversion/multiple. Green circle: d660 conversion/multiple. Violet triangle: d1000 conversion/multiple.

4 ak135-CCP: 1D Depth Correction and CCP Stack

Here we present results for a CCP stack comprising Pds, PPds and PKPds data corrected to depth using the 1D model ak135 (ak135-CCP), i.e. without migration through a 3D model. Figures S6–S8 show stacking weights at 410 km, 660 km, 1000 km, mantle transition zone depths and thickness in map and cross section. We compare results from ak135-CCP to AFRP20-CCP in Figure S8. Topography on the d410 and d660 in Figures S7 and S8 shows strong correlation, with overall uplift beneath SAF and depression beneath EAR and ETH.

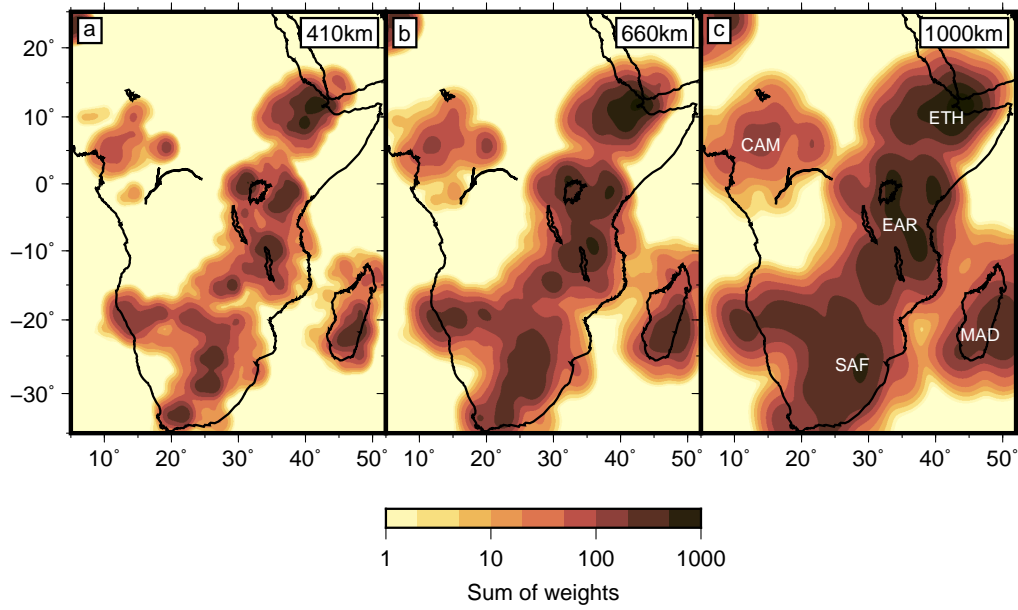**Figure S6.** Stacking weights at 410 km (*a*), 660 km (*b*) and 1000 km (*c*) depth in CCP volumes combining Pds, PPds and PKPds data sets.
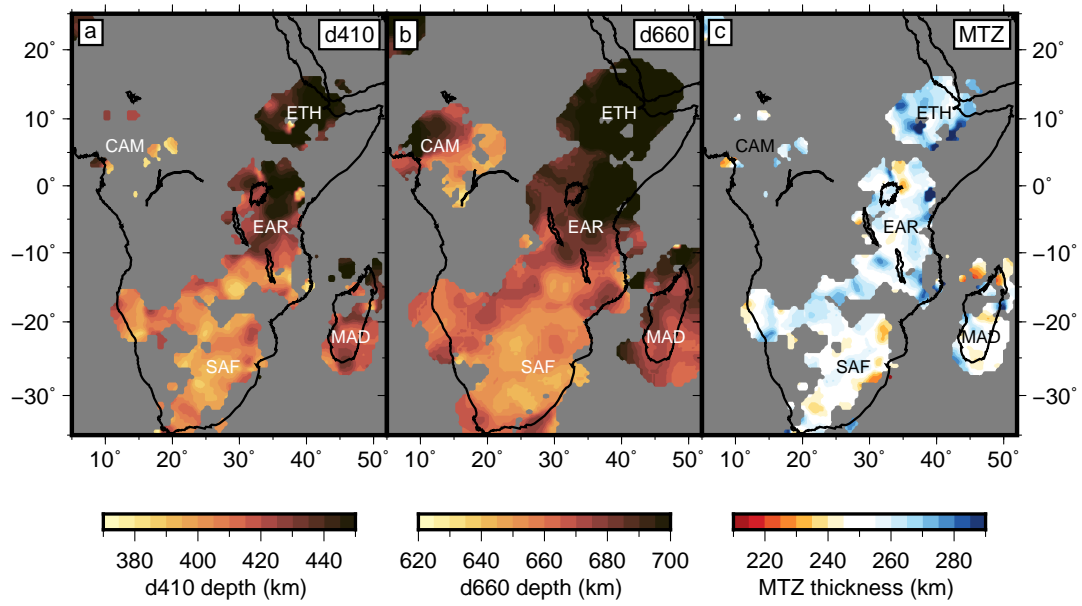
Figure S7. Maps of mantle transition zone (MTZ) discontinuity depths (d410, d660: *a,b*) and thickness (*c*) within ak135-CCP generated using Pds, PPds, PKPds data sets (up to 0.2 Hz). Regions are shown only where stacking weight (Figure S6) and standard error are greater than two.
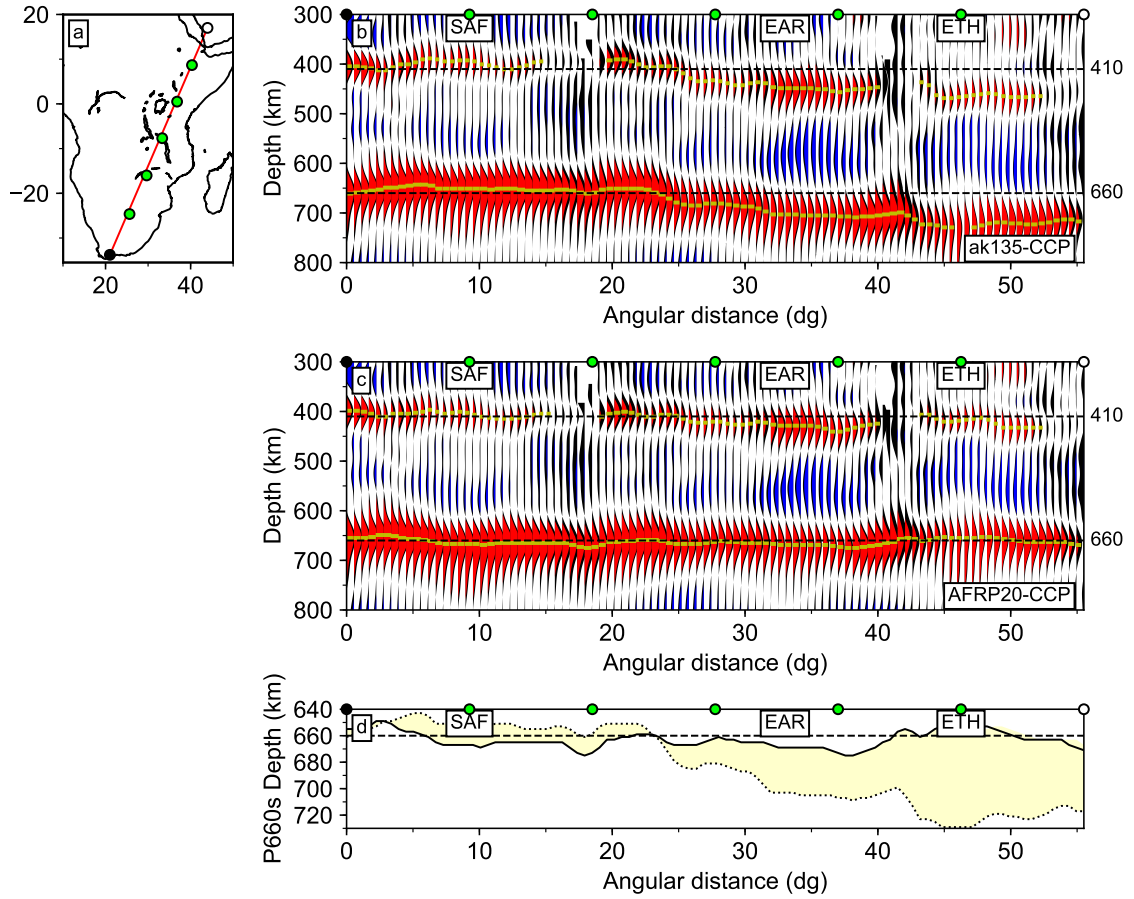
Figure S8. Along the profile (*a*), waveform cross-sections through ak135-CCP (*b*) and AFPR20-CCP (*c*). Yellow ticks: depths of maximum amplitudes of MTZ discontinuities within regions where stacking weight (Figure S6) and standard error is greater than two. RFs calculated up to a maximum frequency of 0.2 Hz. The difference between the 660 km discontinuity depths within ak135-CCP (dashed) and AFRP20-CCP (solid) is highlighted in yellow (*d*).

5 3D Depth Correction and CCP Stacks

We utilize five recent tomographic models within 3D time-to-depth correction and subsequent stacking (AFRP20, AF2019, SL2013SV, SEMUCB-WM1 and SGLOBErani: Boyce et al., 2021; Celli et al., 2020; Schaeffer & Lebedev, 2013; French & Romanowicz, 2014; Chang et al., 2015). Figures S9–S10 compare the d410 and d660 depths from ak135-CCP with that obtained from five 3D time-to-depth corrected CCP stacks: AFRP20-CCP, AF2019-CCP, SL2013-CCP, SEMUCB-CCP, SGLOBErani-CCP. These figures accompany Figure 5 in the main manuscript documenting the variability in MTZ thickness for these six CCP stacks. In Figures S11–S12 we show the mean and standard deviation of d410 depth, d660 depth and MTZ thickness obtained from all five 3D time-to-depth corrected CCP stacks. Average d410 depths beneath ETH are ∼415 km and ∼423 km beneath EAR. Average d660 depths in ETH are ∼659 km and ∼666 km in EAR. d660 discontinuity depths exhibit greatest uncertainty below CAM, northern MAD, central SAF, eastern EAR and the periphery of ETH. The mean discontinuity depths and associated errors arising from variable time-to-depth corrections show a clear difference between discontinuity depths below ETH and EAR (Figure S13). EAR exhibits deeper mean discontinuity depths for both d410 and d660 than ETH.

Figure S9. Maps of d410 discontinuity depths within ak135-CCP (*a*), AFRP20-CCP (*b*), AF2019-CCP (*c*), SL2013-CCP (*d*), SEMUCB-CCP (*e*), SGLOBErani-CCP (*f*) using RF data containing maximum frequencies of 0.2 Hz. Regions are shown only where stacking weight is greater than 2 (Figure S6) and relative amplitude is greater than two standard error. CAM: Cameroon, ETH: Ethiopia, EAR: East African Rift, SAF: Southern Africa, MAD: Madagascar.
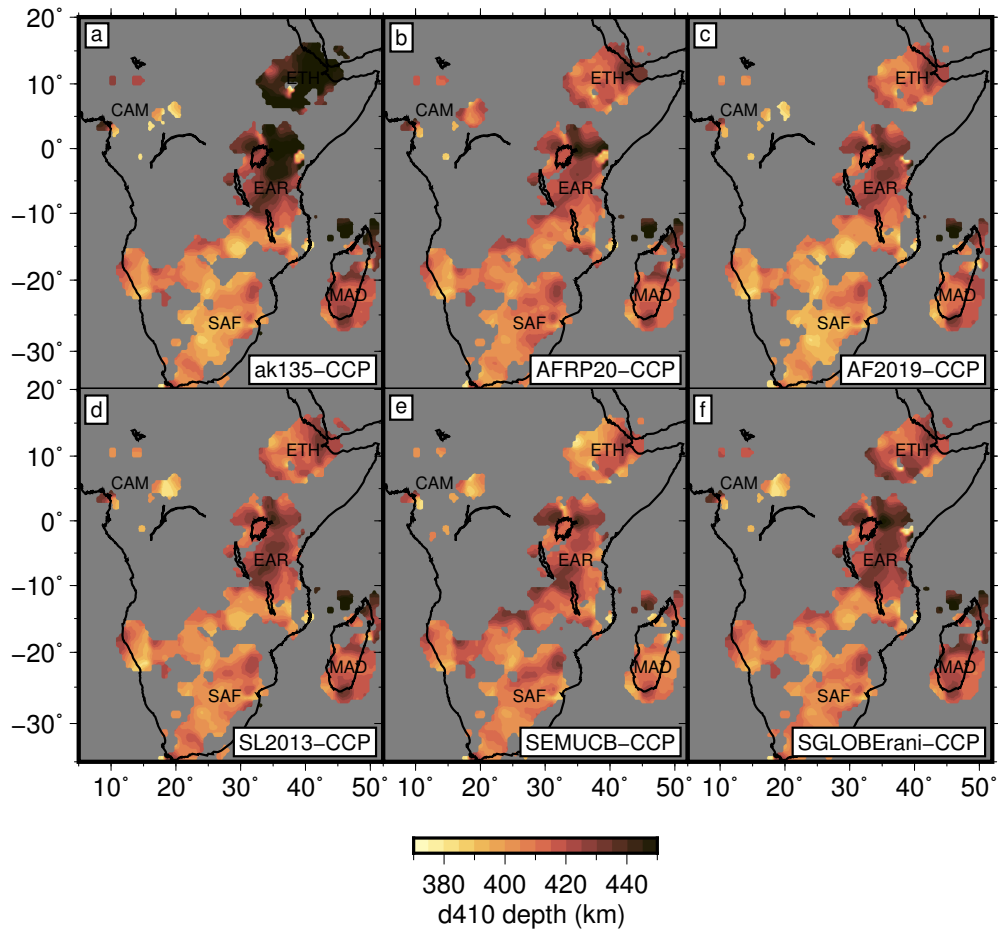
Figure S10. Maps of d660 discontinuity depths within ak135-CCP (*a*), AFRP20-CCP (*b*), AF2019-CCP (*c*), SL2013-CCP (*d*), SEMUCB-CCP (*e*), SGLOBErani-CCP (*f*) using RF data containing maximum frequencies of 0.2 Hz. Regions are shown only where stacking weight is greater than 2 (Figure S6) and relative amplitude is greater than two standard error. CAM: Cameroon, ETH: Ethiopia, EAR: East African Rift, SAF: Southern Africa, MAD: Madagascar.
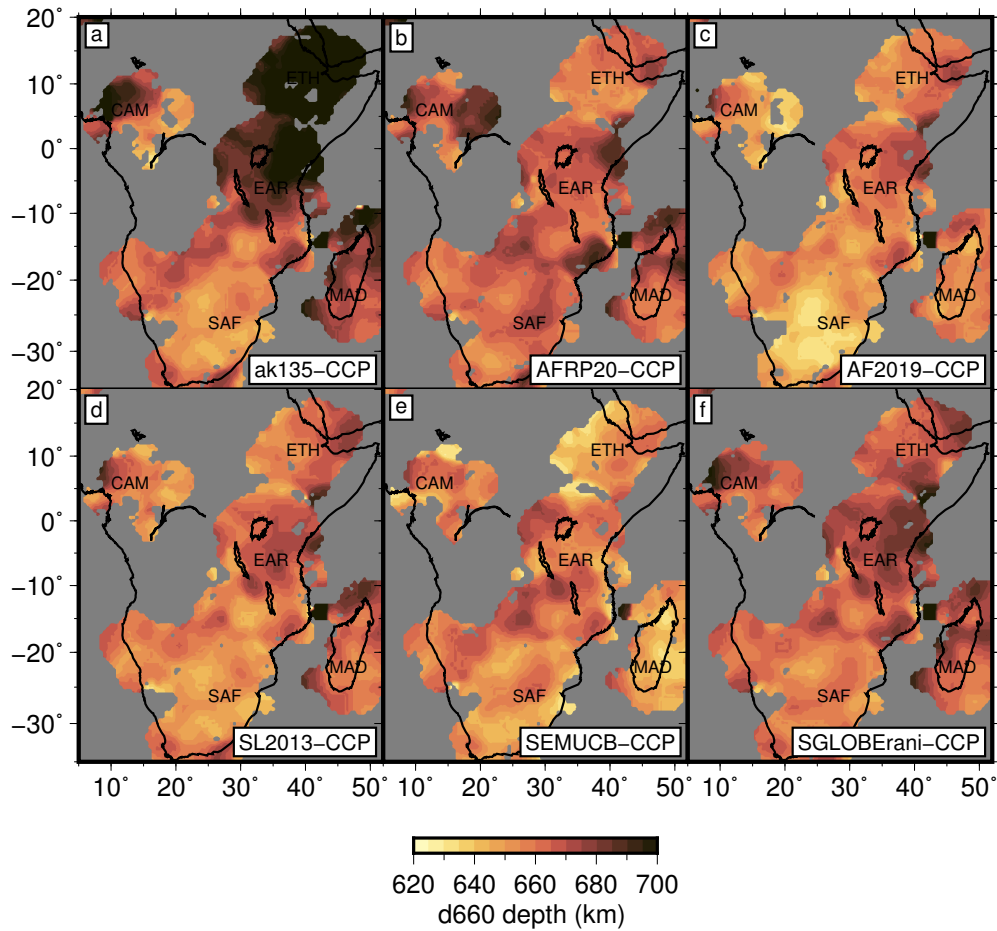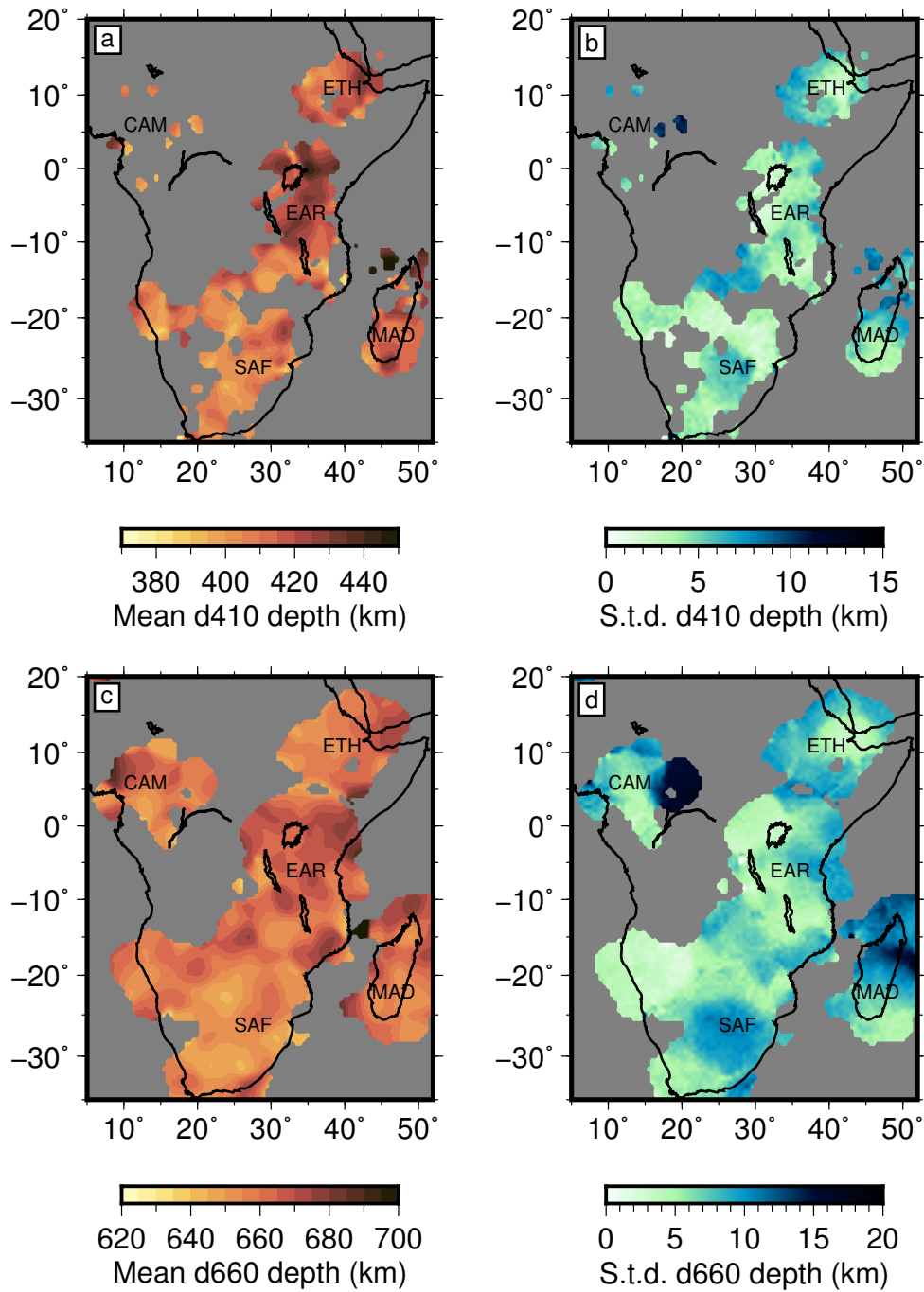
Figure S11. Maps of mean (*a,c*) and standard deviation (*b,d*) of d410 and d660 discontinuity depths obtained from five 3D time-to-depth corrected CCP stacks: AFRP20-CCP, AF2019-CCP, SL2013-CCP, SEMUCB-CCP, SGLOBErani-CCP. RF data contains maximum frequencies of 0.2 Hz. Regions are shown only where stacking weight is greater than 2 (Figure S6) and relative amplitude is greater than two standard error for all five CCP stacks. CAM: Cameroon, ETH: Ethiopia, EAR: East African Rift, SAF: Southern Africa, MAD: Madagascar.

Figure S12. Maps of mean (*a*) and standard deviation (*b*) of MTZ thickness obtained from five 3D time-to-depth corrected CCP stacks: AFRP20-CCP, AF2019-CCP, SL2013-CCP, SEMUCB-CCP, SGLOBErani-CCP. RF data contains maximum frequencies of 0.2 Hz. Regions are shown only where stacking weight is greater than 2 (Figure S6) and relative amplitude is greater than two standard error for all five CCP stacks. CAM: Cameroon, ETH: Ethiopia, EAR: East African Rift, SAF: Southern Africa, MAD: Madagascar.
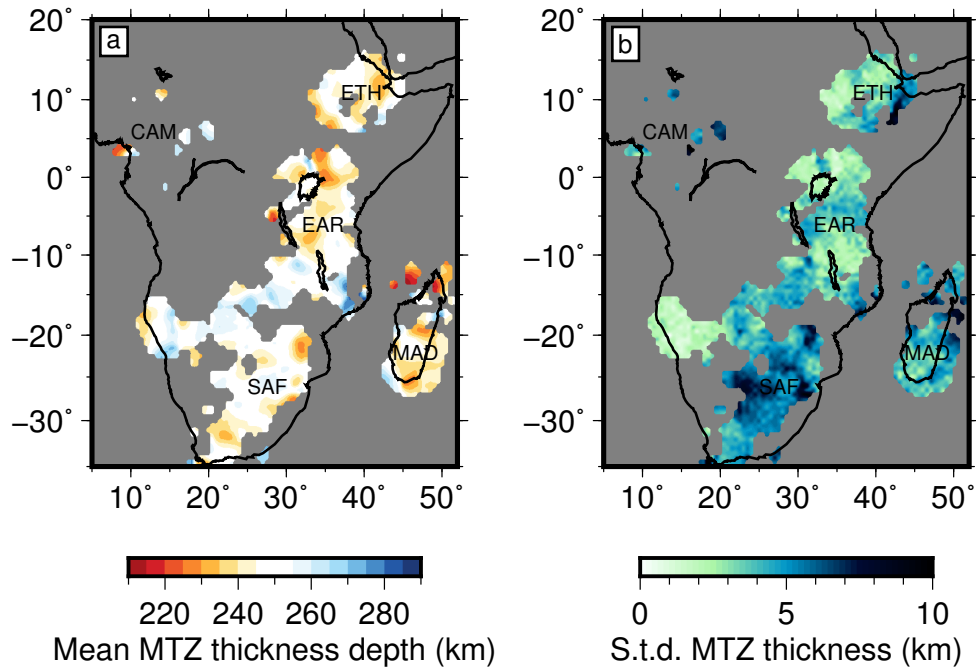
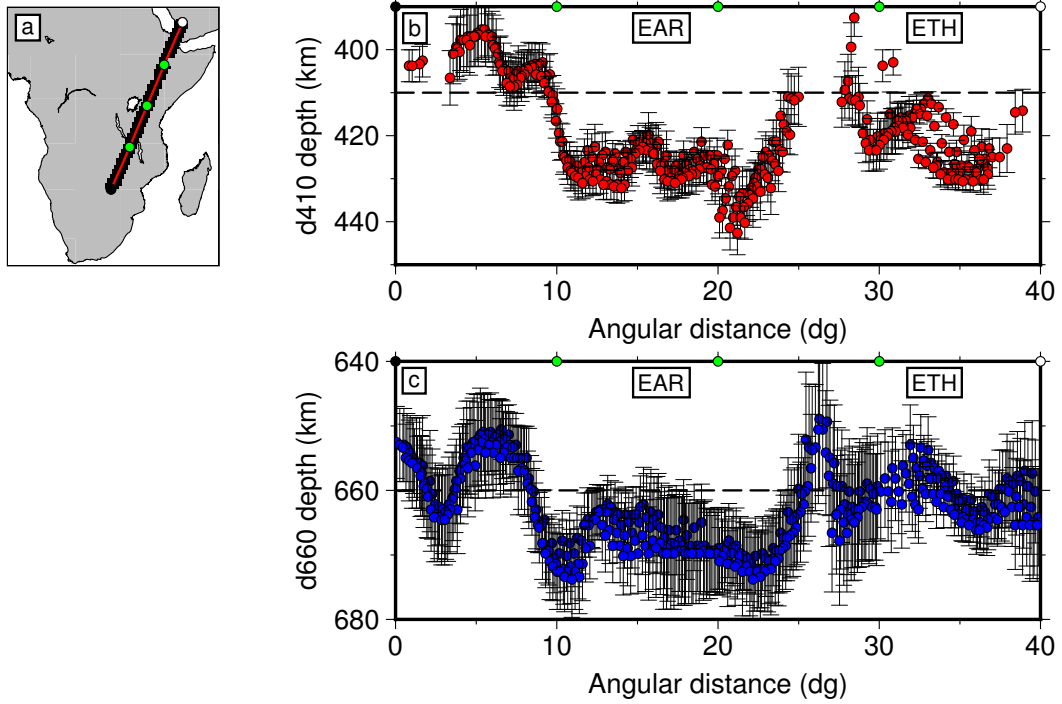**Figure S13.** All d410 and d660 sampling points (black squares) in the mean CCP stack (Figure S11) within 150 km of the profile shown in (*a*) are projected into plane in subfigures (*b,c*). Point-wise mean d410 (red) and d660 (blue) depths are shown with the standard deviation arising from variable time-to-depth corrections from five tomographic models, plotted as error bars. ETH: Ethiopia, EAR: East African Rift.

6 Quantitative Depth Correction Assessment

6.1 Under-or-over Correction of Discontinuity Topography

In Figure S14, we demonstrate the effects of under-and-over correction of MTZ discontinuity topography in a region of warm upper mantle (slow wavespeeds). It is challening to assess if true MTZ discontinuity depths are obtained due to potential errors in the RF data and time-to-depth correction implementation. Tomographic models often used in time-to-depth migration typically suffer both raypath smearing and underestimation of anomaly amplitudes. As such time-to-depth corrected RFs yield apparent discontinuity depths that are often under corrected for anomalies in the upper mantle. In a region where no thermal and compositional perturbations are expected in the MTZ, we can compare the imaged apparent depths of MTZ discontinuities with our expectation of little-to-no topography on the MTZ discontinuities. Figure S14 demonstrates that any under-or-over correction would lead to correlated topography on the d410 and d660 and this forms the conceptual basis for our quantitative analysis below. The effect is reversed for regions of cool upper mantle (fast wavespeeds). We do not expect to reduce apparent topography to zero in regions of MTZ through-going wavespeed anomalies such as mantle plume and subduction zone environments.

Figure S15 demonstrates the impact of 3D slow wavespeed heterogeneity on apparent discontinuity depths derived from 1D and 3D time-to-depth corrections. An anomaly of appropriate amplitude smeared to below 410 km depth will leave spurious residual depressed topography on the d410 (Figure S15a). Inadequate account for anomalies confined to well within the MTZ will yield spurious depressed topography on the d660 (Figure S15b). In the case of slow wavespeeds traversing the MTZ we expect to decipher between dominant mineralogical compositions by the differing behavior of the d660 after 3D time-to-depth correction (Figure S15c,d).

6.2 Initial Correlations

We quantitatively analyze the topography resulting using different tomographic models following (van Stiphout et al., 2019). To do this, we extract values for d410 and d660 depths at CCP grid points where both standard error and summed stacking weights, reported by all six CCP volumes (ak135-CCP, AFRP20-CCP, AF2019-CCP, SL2013-CCP,
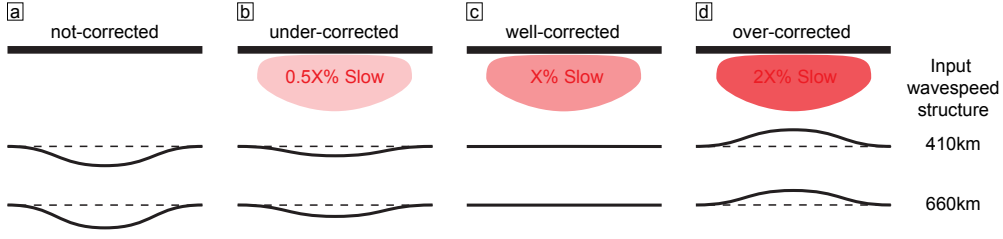
Figure S14. Sketch to illustrate no correction (*a*), under correction (*b*), appropriate correction (*c*) and over correction (*d*) of MTZ topography in a region of slow upper mantle wavespeeds that does not extend into the MTZ. X% is the appropriate seismic wavespeed anomaly (δV) for the upper mantle that reduces apparent topography (solid line) on the d410 and d660 to zero (true depth: dashed lines) as expected for a MTZ without thermal perturbation. The effect is reversed for regions of fast upper mantle wavespeeds. The vertical scale is exaggerated significantly.
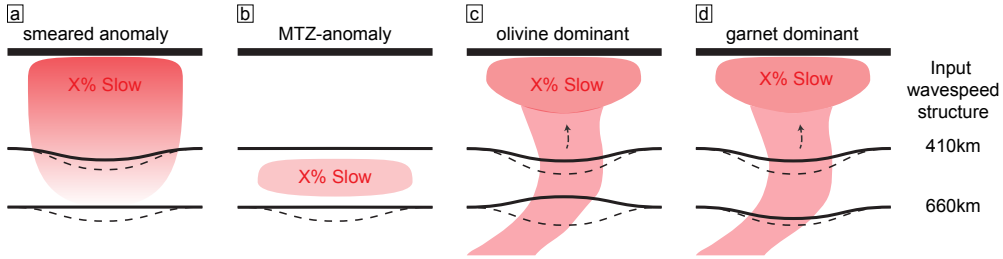

Figure S15. Sketch to illustrate the impact of 3D wavespeed heterogeneity on apparent discontinuity depths when imaged using a 1D (dashed line) and 3D time-to-depth correction (solid line). The scenarios shown are: (*a*) a smeared slow wavespeed anomaly to below 410 km depth, (*b*) a slow wavespeed anomaly within the MTZ not interacting with the upper and lower discontinuities, (*c*) an olivine dominant anomaly traversing the MTZ and (*d*) a garnet dominant anomaly traversing the MTZ. X% is the appropriate seismic wavespeed anomaly (δV) that yields the true topography on the d410 and d660. The vertical scale is exaggerated significantly.

SEMUCB-CCP, SGLOBErani-CCP), are greater than 2 (Figure S6). We define relative depths ($d^R 410$, $d^R 660$) as the discontinuity depth compared to the global average of 410 km or 660 km:

$$d^R 410 = d410 - 410 \tag{1}$$

$$d^R 660 = d660 - 660 \tag{2}$$

We define positive to be greater depth i.e. downwards. Next, we define the d410 and d660 corrections ($c410$, $c660$) by comparing the depths of $d^{3D}410$ and $d^{3D}660$ discontinuities in the CCP stacks based on 3D tomographic models with those from the 1D velocity model:

$$c410 = d^{3D}410 - d^{1D}410 \tag{3}$$

$$c660 = d^{3D}660 - d^{1D}660 \tag{4}$$

Positive corrections exist when the discontinuity using a 3D tomographic model is deeper than that obtained using a 1D tomographic model, i.e. accounting for 3D upper mantle wavespeed structure moved the discontinuity to greater depth. Negative corrections exist when the discontinuity using a 3D tomographic model is shallower than that obtained using a 1D tomographic model, i.e. accounting for 3D upper mantle wavespeed structure moved the discontinuity to shallower depth. For example, a fast wavespeed through-going structure such as a subducting slab will enable converted phases above the discontinuity to travel faster than that predicted by a 1D model. In such a region, a 1D model will predict shallow discontinuities for a given converted arrival with respect to the direct P-wave because the time between these arrivals is lower than expected. Since the converted phase has traveled faster during its ascent (based on the 3D wavespeed model), we move the discontinuity to greater depth to account for this. We define this as a positive discontinuity correction. Conversely, a slow wavespeed through-going structure such as a mantle plume will reduce the wavespeed of converted phases above the discontinuity with respect to a 1D model. A 1D model will predict deep discontinuities for a given converted arrival with respect to the direct P-wave because the time between arrivals is higher than expected. Since the converted phase has traveled slower during its ascent (based on the 3D wavespeed model), we move the discontinuity to shallower depth to account for this. We define this as a negative discontinuity correction.

We measure the linear correlation between three sets of variables, using the Pearson correlation co-efficient or Pearson's **r** value. We refer to this as the **r** value from here onward:

1. Relative d410 depth and relative d660 depth : $\mathbf{r}[d^R410 : d^R660]$
2. Relative d410 depth and 410 correction : $\mathbf{r}[d^R410 : c410]$

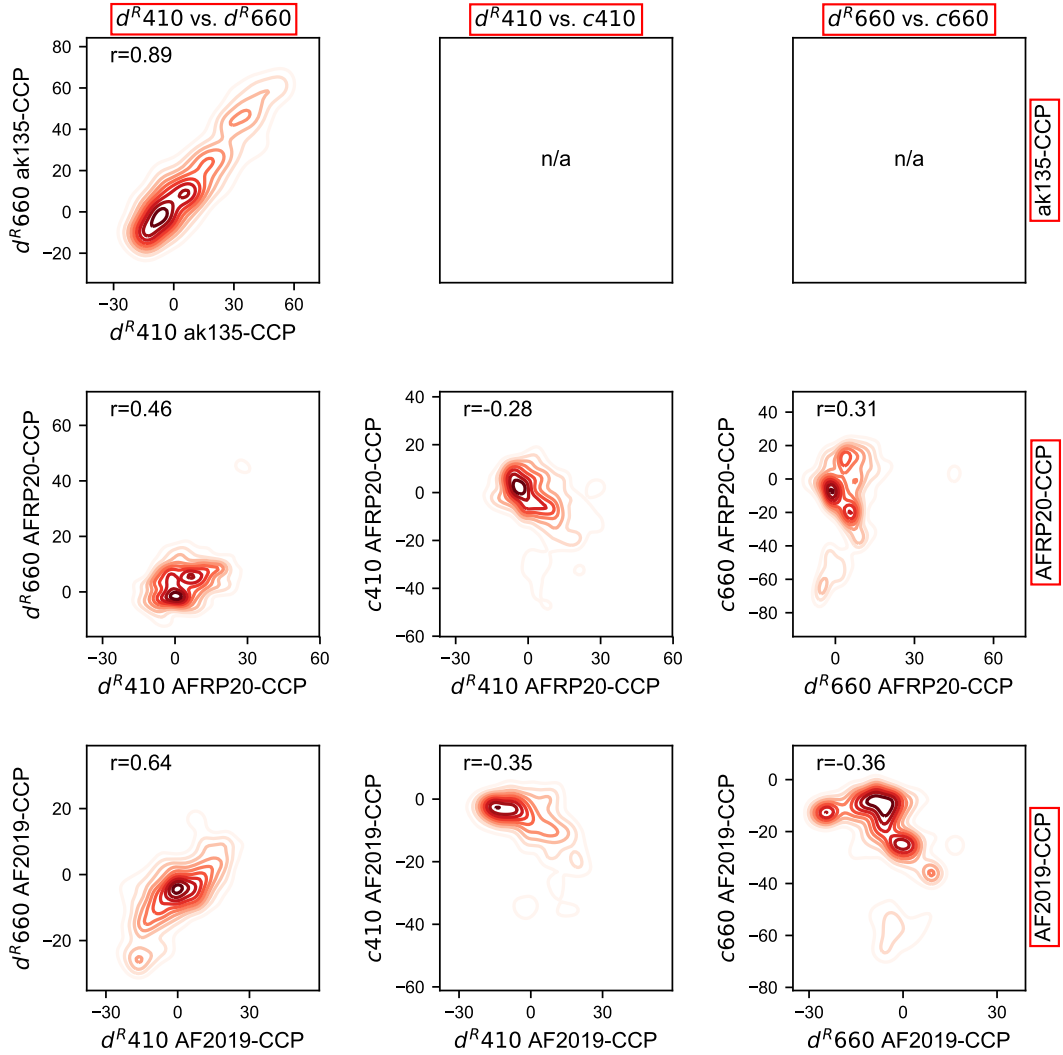3. Relative d660 depth and 660 correction : $\mathbf{r}[d^R660 : c660]$

Figure S16. Plot of $\mathbf{r}[d^R410 : d^R660]$, $\mathbf{r}[d^R410 : c410]$ and $\mathbf{r}[d^R660 : c660]$ for MTZ discontinuities in ak135-CCP, AFRP20-CCP, AF2019-CCP Definitions are given in the text.

Figure S16 shows the correlation contour plots for these three sets of variables for three of our CCP stacks: ak135-CCP, AFRP20-CCP, AF2019-CCP. Because both MTZ discontinuities will be shallow using a 1D velocity model in regions of fast upper mantle wavespeeds and deep in regions of slow upper mantle wavespeeds, we expect high $\mathbf{r}[d^R410 : d^R660]$ when upper mantle velocities are inadequately or incorrectly accounted for. For a mantle transition zone consisting of pure olivine we would expect $\mathbf{r}[d^R410 : d^R660]$ <0. The positive Clapeyron slope of the 410 km discontinuity results in deeper d410 in

warm environments and shallower d410 in cold environments. The negative Clapeyron slope of the olivine dominant 660 km discontinuity results in a shallow d660 in warm environments and a deep d660 in cold environments. However in the warmest regions, the garnet transition can become significant at the base of the MTZ. This transition has a positive Clapeyron slope so d660 becomes deeper here, thus regionally we might expect $\mathbf{r}[d^R410 : d^R660] > 0$. On the whole though, we seek 3D tomographic wavespeed models that minimize $\mathbf{r}[d^R410 : d^R660]$.

It is also worth thinking about what correlations we expect between discontinuity topography and the corrections thereof, assuming some correlations in thermal anomalies across the upper mantle and transition zone. Warm environments are typically characterized by slow upper mantle velocities. Due to the positive Clapeyron slope of the 410 km discontinuity, $c410$ will be negative but d^R410 will be positive, (i.e. $d^{3D}410 > 410$ km). Conversely cold environments are characterized by high upper mantle velocities. Here, $c410$ will be positive, but d^R410 will be negative (i.e. $d^{3D}410 < 410$ km). We therefore seek a 3D tomographic model that results in $\mathbf{r}[d^R410 : c410] \leq 0$.

In an olivine dominated warm mantle, characterized by slow velocities, the negative Clapeyron slope of the 660 km results in a negative $c660$, whilst d^R660 will also be negative (i.e. $d^{3D}660 < 660$ km). In an olivine dominated cold mantle, characterized by fast velocities, $c660$ will be positive, whilst d^R660 will also be positive (i.e. $d^{3D}660 > 660$ km). For the olivine system both the relative depth and correction at the 660 take the same sign so we expect a $\mathbf{r}[d^R660 : c660] \geq 0$.

At very high temperatures where the garnet transition becomes significant at the 660 km discontinuity, the Clapeyron slope is positive, so locally we could expect $\mathbf{r}[d^R660 : c660] \leq 0$. Finally, in regions where upper mantle and transition zone thermal anomalies are uncorrelated we expect no significant correlations for $\mathbf{r}[d^R410 : c410]$ and $\mathbf{r}[d^R660 : c660]$. There is no specific reason to expect anti-correlated thermal anomalies in the upper mantle and transition zone.

Figure S16 shows ak135-CCP to have very high $\mathbf{r}[d^R410 : d^R660] = 0.89$ and is therefore not preferable. AFRP20-CCP displays a low $\mathbf{r}[d^R410 : d^R660] = 0.46$ and values of $\mathbf{r}[d^R410 : c410] = -0.28$ and $\mathbf{r}[d^R660 : c660] = 0.31$ with approximately equal magnitude and opposite sign. This indicates good performance of depth corrections for both the d410 and d660 using AFRP20 (Boyce et al., 2021). AF2019-CCP shows

a moderate $\mathbf{r}[d^R410 : d^R660] = 0.64$ and negative values for both $\mathbf{r}[d^R410 : c410] = -0.35$ and $\mathbf{r}[d^R660 : c660] = -0.36$. The negative value for $\mathbf{r}[d^R660 : c660]$ indicates an inadequacy of d660 depth corrections applied by AF2019 when assuming most of the d660 behavior is controlled by olivine.

Results for other CCP stacks are as follows – SL2013-CCP: $\mathbf{r}[d^R410 : d^R660] = 0.63$, $\mathbf{r}[d^R410 : c410] = -0.31$ and $\mathbf{r}[d^R660 : c660] = -0.34$; SEMUCB-CCP: $\mathbf{r}[d^R410 : d^R660] = 0.52$, $\mathbf{r}[d^R410 : c410] = 0.05$ and $\mathbf{r}[d^R660 : c660] = 0.32$; SGLOBErani-CCP: $\mathbf{r}[d^R410 : d^R660] = 0.61$, $\mathbf{r}[d^R410 : c410] = -0.36$ and $\mathbf{r}[d^R660 : c660] = -0.40$. By these quantitative measures, AFRP20 offers the most preferable time-to-depth corrections for the tomographic models tested here, as it displays the lowest $\mathbf{r}[d^R410 : d^R660]$, as well as the only model to display opposite correlations between the $\mathbf{r}[d^R410 : c410]$ and $\mathbf{r}[d^R660 : c660]$.

6.3 Rescaling Topographic Corrections

Next we assess whether topographic corrections applied by the five 3D tomographic models (AFRP20, AF2019, SL2013SV, SEMUCB-WM1, SGLOBErani) are appropriate based on the criteria defined above or could be improved by rescaling corrections, since tomographic models typically locate wavespeed anomalies well, but can underestimate anomaly amplitudes. The corrections for upper mantle anomalies can also be over or underestimated due to our assumed scaling between δV_P and δV_S wavespeed anomalies. We linearly re-scale the topographic depth corrections ($c410$ and $c660$) applied by each 3D tomographic model from 0.5–1.9 and measure the resulting correlations between parameters. While linearly re-scaling the corrections may not be as comprehensive as re-scaling each wavespeed model and re-running multiple CCP stacks we suggest this is likely a good approximation to that behavior and hence sufficient for our purposes.

Figure S17 shows a range of linear re-scaling factors against the correlation statistics for the three sets of variables discussed above. The sweet spot highlights the range of re-scaling factors that can suitably fit our criteria outlined previously, with the best fitting re-scaling factor shown by the dashed line. Following van Stiphout et al. (2019) we select the ideal topographic correction factors using the lowest $\mathbf{r}[d^R410 : d^R660]$ and similar magnitudes of $\mathbf{r}[d^R410 : c410]$ and $\mathbf{r}[d^R660 : c660]$ but with opposing sign be-

cause we expect the phase transitions at d410 and d660 to have roughly similar Clapeyron slopes of opposite sign in an olivine dominated mantle.

Figure S17a shows a broader range of appropriate re-scaling factors from 0.9–1.2 for AFRP20-CCP. Variation in $\mathbf{r}[d^R410 \ : \ d^R660]$ is low within the sweet spot region and thus following the criteria above the best fitting scaling factor is 1.0 where $\mathbf{r}[d^R410 : c410]$ and $\mathbf{r}[d^R660 : c660]$ have similar magnitudes of opposing sign. This indicates that depth corrections across Africa are good on average and that wavespeed anomalies within the AFRP20 tomographic model are appropriate for MTZ discontinuity topographic correction.

Figure S17b shows that the most appropriate re-scaling factor for AF2019-CCP is 1.3. This suggests that discontinuity depths within AF2019-CCP are slightly undercorrected across Africa on average. In turn, this indicates that wavespeed anomaly amplitudes are slightly underestimated beneath Africa in the AF2019 tomographic model. The most appropriate re-scaling factor for SL2013-CCP is 1.2 and for SGLOBErani-CCP is 1.3 (Figure S17c,e). This again indicates slight undercorrection of discontinuities for these CCP stacks. Underestimation of anomaly amplitudes in these tomographic models is consistent with the damped least squares inverse approaches used within these inversions (Schaeffer & Lebedev, 2013; Chang et al., 2015). SEMUCB-CCP indicates the most appropriate re-scaling factor may be 0.9 which is consistent with stronger anomaly amplitudes that typically result from waveform tomography approaches (French & Romanowicz, 2014).
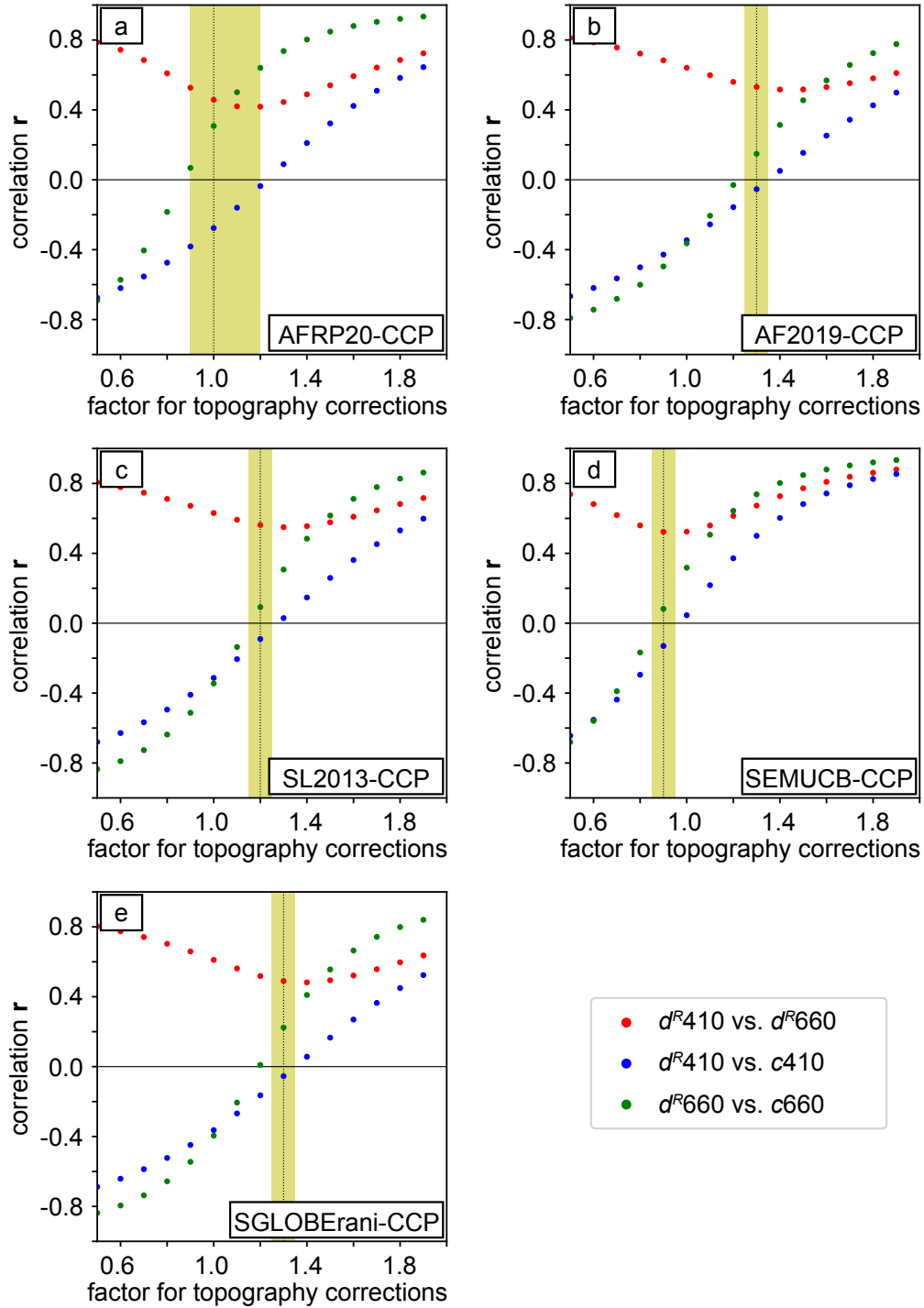
Figure S17. Scatter plots to show the linear topographic scaling factor against the Pearson correlation for $\mathbf{r}[d^R410 : d^R660]$, $\mathbf{r}[d^R410 : c410]$ and $\mathbf{r}[d^R660 : c660]$ (red, blue and green dots respectively) for five CCP stacks derived from 3D time-to-depth corrections AFRP20-CCP (*a*), AF2019-CCP (*b*), SL2013-CCP (*c*), SEMUCB-CCP (*d*), SGLOBErani-CCP (*e*). The sweet spot for the topographic scaling factor is highlighted in yellow with best fitting scaling factor shown by the dashed vertical line. Definitions are given in the text.

7 AFRP20-CCP Frequency Testing

Figures S18 and S19 show d410 and d660 depths for AFRP20-CCP across a range of RF maximum frequencies (0.2–0.9 Hz). Please see Figure 6 in main manuscript for the corresponding cross sections. Note that the d410 in Figure S18 does not change as a function of frequency, whilst the d660 varies beneath EAR in Figure S19.
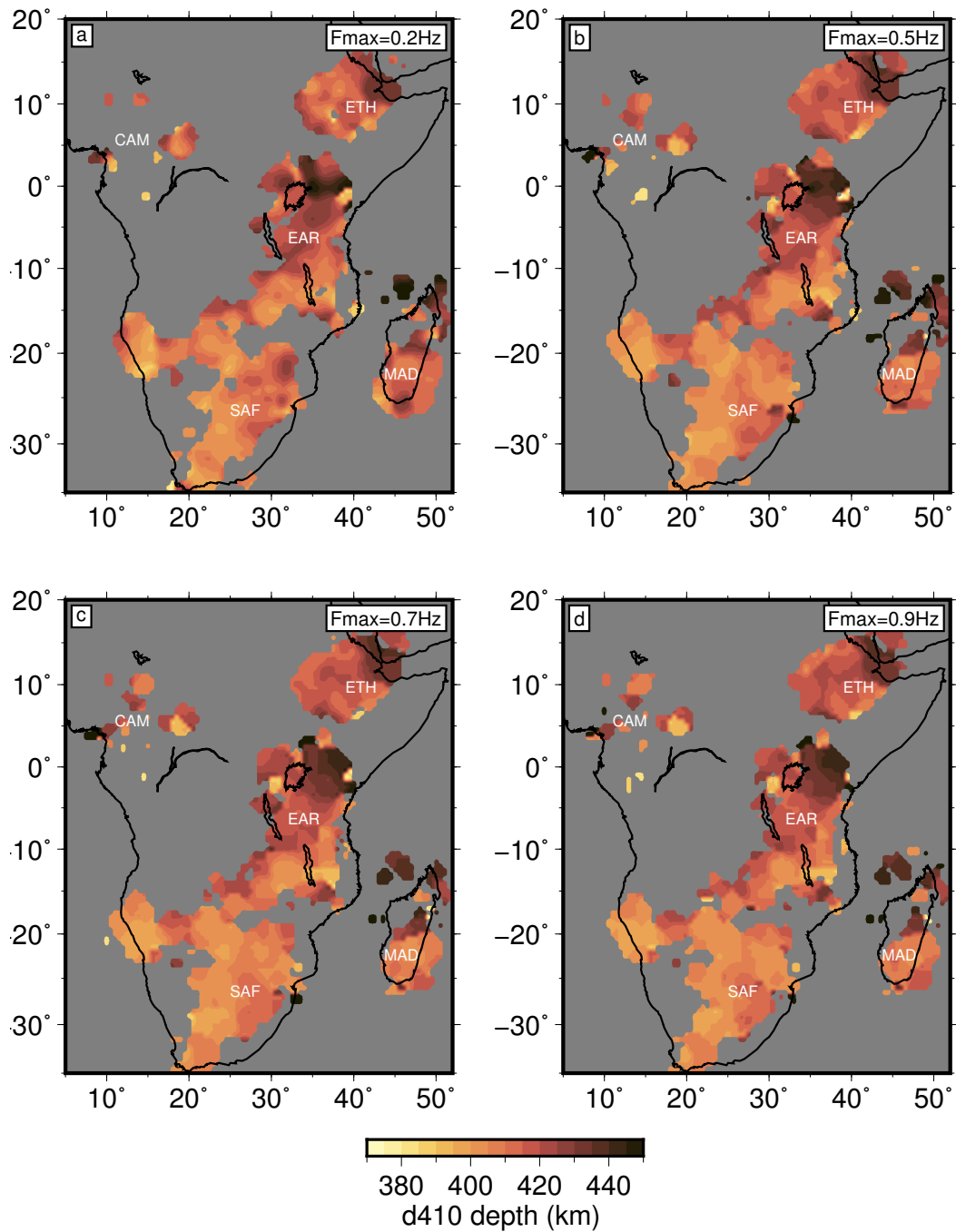
Figure S18. Maps of d410 depth for AFRP20-CCP computed using RFs with maximum frequencies ranging from 0.2–0.9 Hz ($a–d$).
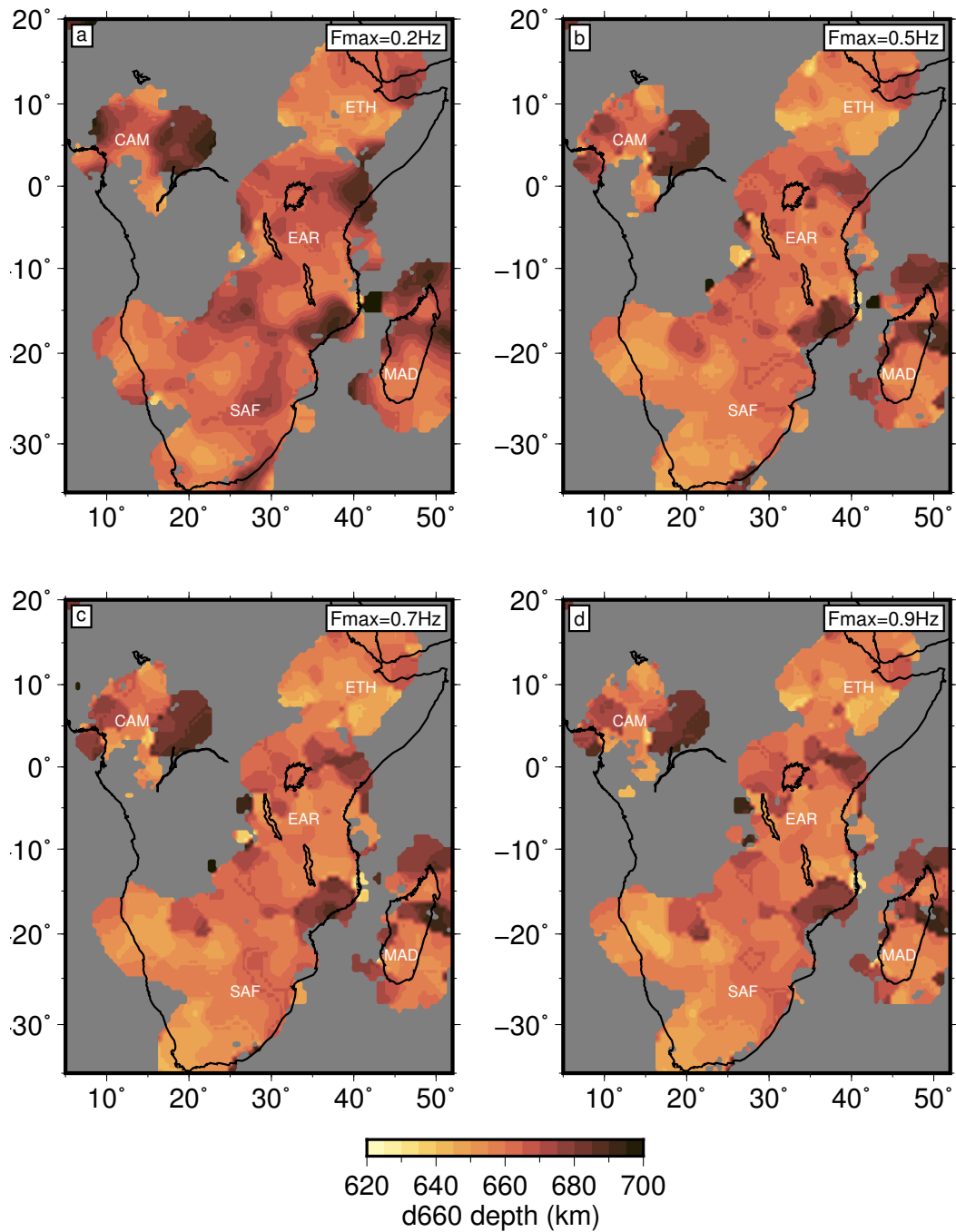
Figure S19. Maps of d660 depth for AFRP20-CCP computed using RFs with maximum frequencies ranging from 0.2–0.9 Hz (*a–d*).

8 Mantle Transition Zone Discontinuity Values

For the regions defined by the latitude and longitude bounds given in Table S1, we give median, mean and standard deviation of d410, d660 depths and MTZ thicknesses within AFRP20-CCP, AF2019-CCP, SL2013-CCP, SEMUCB-CCP and SGLOBErani-CCP in Tables S2–S4. We report values for CCP stacks generated using a maximum RF frequency of $0.2\,$Hz and a two Fresnel zone half width smoothing. These regional bounds are also used in presentation of depth and slowness stacks shown in Section 3.

Regional bounds				
Region	Min. Lon. (°)	Max. Lon. (°)	Min. Lat. (°)	Max. Lat. (°)
AFR	5	52	-35	20
CAM	7	21	-2	12
ETH	34	45	5	15
EAR	28	40	-10	3
SAF	15	33	-35	-20
MAD	43	51	-25	-10

Table S1. Latitude and longitude bounds used for each region reporting d410, d660 depths and MTZ thickness, depth and slowness stacks.

CCP d410 depths (km)															
Region	AFRP20-CCP			AF2019-CCP			SL2013-CCP			SEMUCB-CCP			SGLOBErani-CCP		
	MED.	MN.	S.T.D.	MED.	MN.	S.T.D.	MED.	MN.	S.T.D.	MED.	MN.	S.T.D.	MED.	MN.	S.T.D.
AFR	412.6	414.3	11.6	408.6	409.4	12.8	412.6	412.8	12.3	410.6	411.7	10.6	414.6	415.0	12.7
CAM	414.6	413.5	12.8	396.5	400.7	15.2	399.5	400.9	14.7	401.6	402.2	11.1	398.5	404.3	17.5
ETH	416.6	416.8	9.1	412.6	413.3	8.7	414.6	415.3	9.0	408.6	408.0	10.7	418.6	418.0	9.1
EAR	420.6	422.4	10.3	420.6	420.9	8.8	422.6	423.2	7.8	418.6	419.5	9.4	426.6	426.3	10.1
SAF	406.6	407.8	7.4	398.5	400.4	8.3	406.6	406.6	7.8	408.6	408.5	8.0	406.6	407.1	7.0
MAD	414.6	420.8	14.3	416.6	417.6	14.0	418.6	421.6	14.1	408.6	409.8	11.6	420.6	423.5	11.9

Table S2. d410 depths for each region within the five 3D time-to-depth corrected CCP stacks. MED. = Median, MN. = Mean, S.T.D. = Standard Deviation. All values presented in kilometers.

CCP d660 depths (km)

Region	AFRP20-CCP			AF2019-CCP			SL2013-CCP			SEMUCB-CCP			SGLOBErani-CCP		
	MED.	MN.	S.T.D.	MED.	MN.	S.T.D.	MED.	MN.	S.T.D.	MED.	MN.	S.T.D.	MED.	MN.	S.T.D.
AFR	665.0	666.3	10.5	655.0	654.6	10.7	659.0	659.9	10.4	655.0	654.7	10.2	665.0	666.6	10.2
CAM	671.0	671.2	12.0	648.9	650.5	10.9	655.0	657.0	10.1	657.0	655.5	10.2	665.0	667.4	10.7
ETH	657.0	657.9	5.6	657.0	658.0	7.0	661.0	660.8	7.0	651.0	650.2	8.2	667.0	668.2	6.8
EAR	667.0	667.0	6.2	661.0	661.6	6.5	667.0	665.8	6.2	661.0	660.2	8.0	673.0	673.4	6.9
SAF	663.0	662.5	7.2	644.9	644.9	9.0	651.0	652.7	7.0	651.0	651.9	7.4	657.0	657.8	6.0
MAD	669.0	670.8	11.1	655.0	656.9	8.4	663.0	665.9	10.7	644.9	645.7	7.3	671.0	670.6	9.0

Table S3. d660 depths for each region within the five 3D time-to-depth corrected CCP stacks. MED. = Median, MN. = Mean, S.T.D. = Standard Deviation. All values presented in kilometers.

CCP MTZ thickness (km)

Region	AFRP20-CCP			AF2019-CCP			SL2013-CCP			SEMUCB-CCP			SGLOBErani-CCP		
	MED.	MN.	S.T.D.	MED.	MN.	S.T.D.	MED.	MN.	S.T.D.	MED.	MN.	S.T.D.	MED.	MN.	S.T.D.
AFR	250.4	250.4	11.7	244.4	244.2	9.9	246.4	246.2	9.6	244.4	243.3	10.0	250.4	250.6	10.4
CAM	265.4	260.3	16.7	248.4	244.2	12.0	252.4	250.3	12.5	252.4	248.3	15.5	263.4	257.9	15.4
ETH	240.4	241.1	8.1	244.4	244.5	7.7	244.4	245.3	7.9	242.4	242.8	7.6	250.4	250.3	9.0
EAR	244.4	244.8	10.2	240.4	241.5	8.0	244.4	244.0	7.2	240.4	241.0	8.7	248.4	248.0	10.4
SAF	256.4	255.1	7.8	242.4	243.2	8.3	246.4	245.3	8.6	244.4	244.0	8.8	250.4	250.4	8.2
MAD	246.4	246.6	11.8	236.4	237.3	11.0	240.4	241.2	10.7	234.4	234.5	10.3	244.4	244.7	10.9

Table S4. MTZ thickness for each region within the five 3D time-to-depth corrected CCP stacks. MED. = Median, MN. = Mean, S.T.D. = Standard Deviation. All values presented in kilometers.

9 Local Depth and Slowness Stacks for Mid-mantle Features

Figures S20–S24 show Pds data depth and slowness stacks for RFs whose piercing points at 1000 km fall within the given region. Figures S25–S29 show PPds data depth and slowness stacks for the same regions. Depth stacks comprise RFs corrected to depth using the AFRP20 tomographic model (Boyce et al., 2021). Regions used are shown in Figure 7 of the main manuscript and are defined in Table S5. Confidence in a true conversion rather than a multiple is indicated by the region name highlight (green = high, yellow = intermediate, red = low). For a high confidence result we seek a clear positive peak, above error, within the depth stack at 960–1100 km depth as well as a clear positive peak in close proximity to the predicted negative relative slowness for converted phases at ∼95–115 s relative delay time from the direct-P arrival (e.g., Figure S22c,d). Intermediate confidence results typically display an above error positive peak in the depth stack but positive peaks in the slowness stack are either smeared to greater and lesser relative slowness (likely due to limited epicentral distance coverage e.g., Figure S22a,b) or occur at both positive and negative slowness at similar relative delay times (e.g., Figure S21e,f). Low confidence results typically display high error in the depth stack and lack positive peaks at negative relative slowness at the appropriate relative delay time (e.g., Figure S21a,b).

Regional bounds				
Region	Min. Lon. (°)	Max. Lon. (°)	Min. Lat. (°)	Max. Lat. (°)
R1	34	40	14	18
R2	38	40	12	14
R3	45	49	9	13
R4	18	21	2	6.5
R5	30	33	3	6
R6	37	39	1	4
R7	30	34	0	3
R8	30	35	-4	0
R9	33	38	-9	-4
R10	27	31	-15	-10
R11	35	37	-15	-12
R12	40	43	-25	-19
R13	49	52	-25	-20
R14	31	34	-27	-22
R15	16	22	-35	-32

Table S5. Latitude and longitude values used to construct depth and slowness stacks for each region reporting d1000 depths in AFRP20-CCP.
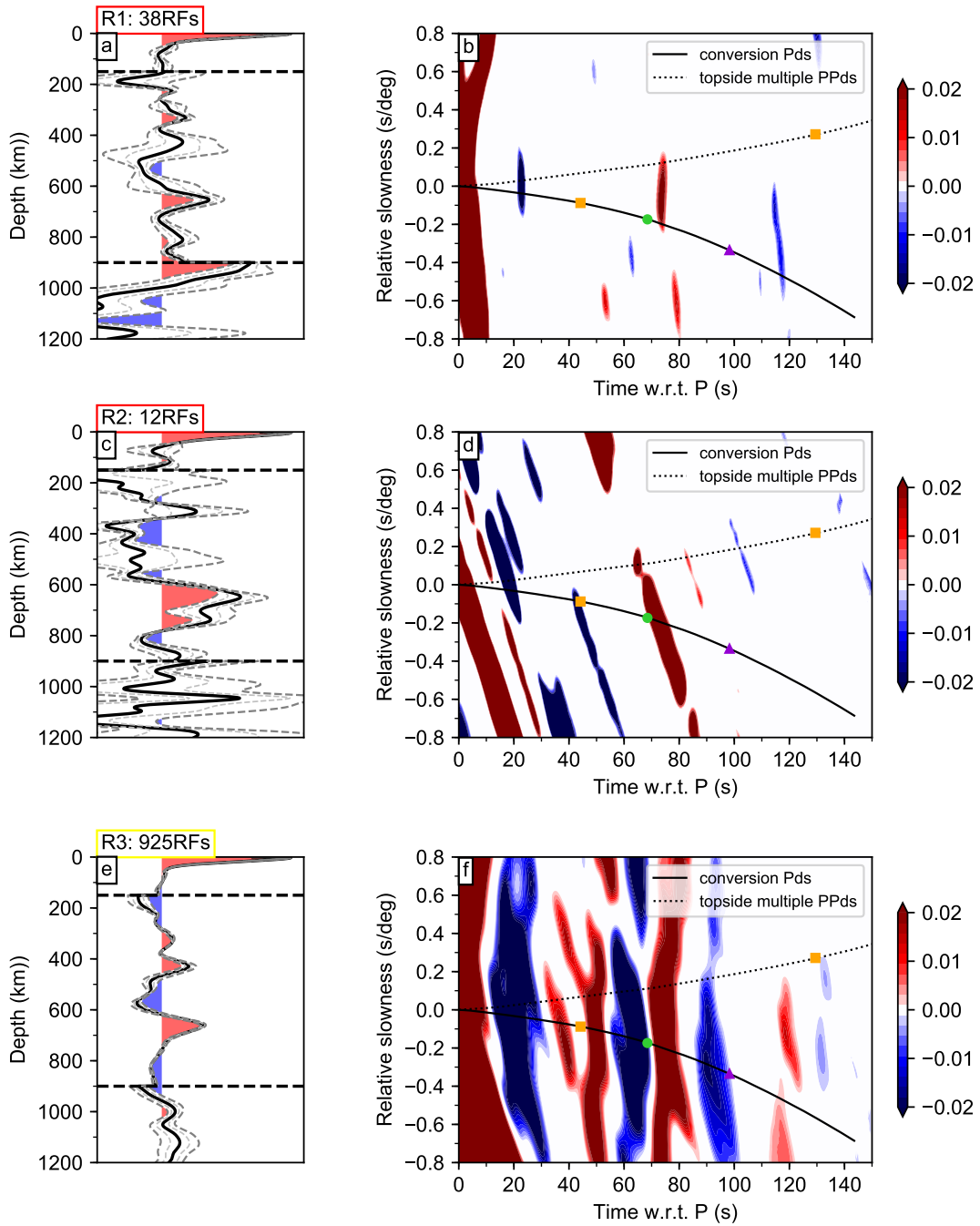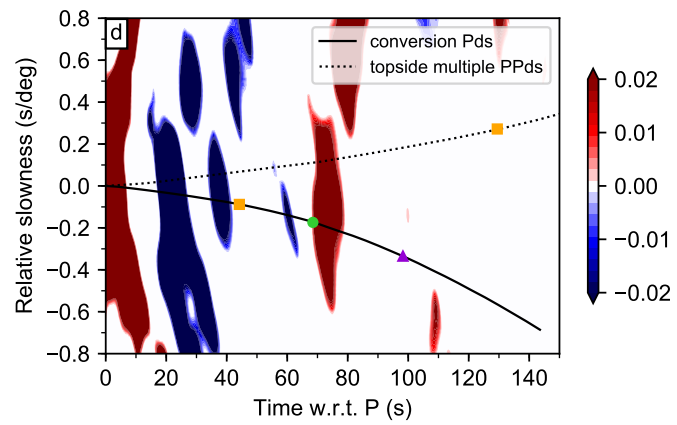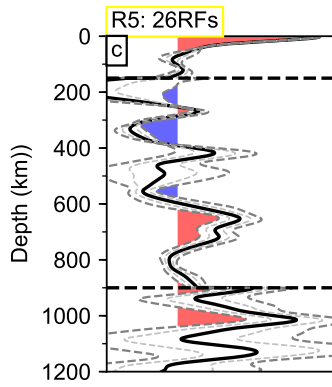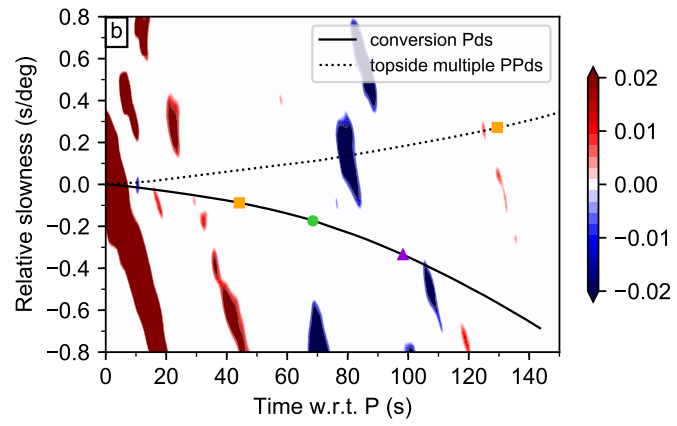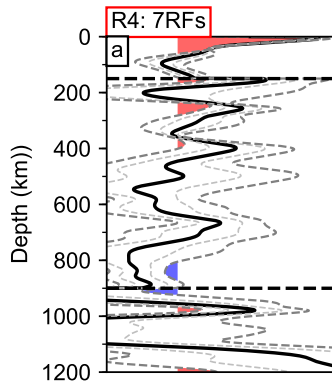
Figure S20. Local depth (a,c,e) and slowness stacks (b,d,f) for Pds data whose piercing points at 1000 km depth fall within in the specified regions R1, R2, R3. Regions are shown in Figure 7 of the main manuscript. RF max frequency is 0.2 Hz. The number of RFs included in the stack is given in the colored upper left box. High confidence result: green, intermediate: yellow, low confidence: red. Depth stacks comprise RFs corrected to depth using the AFRP20 tomographic model (Boyce et al., 2021). Depth stack amplitudes are multiplied by five and twenty below 150 km and 900 km respectively. Predicted converted Pds arrivals have negative slowness (solid line), multiples have positive slowness (dashed line) w.r.t. direct-P phase. Orange square: d410 conversion/multiple. Green circle: d660 conversion/multiple. Violet triangle: d1000 conversion/multiple.
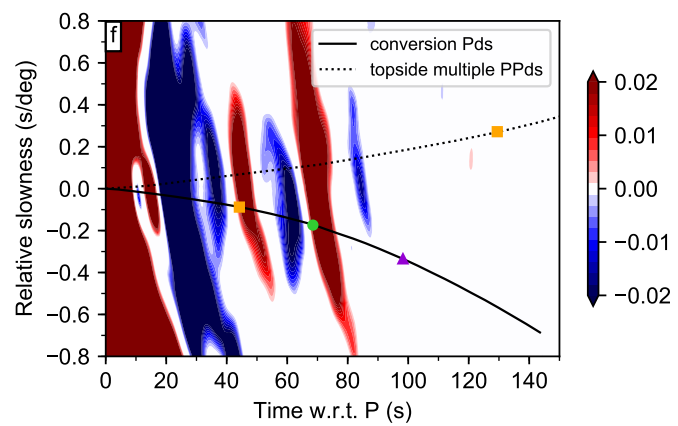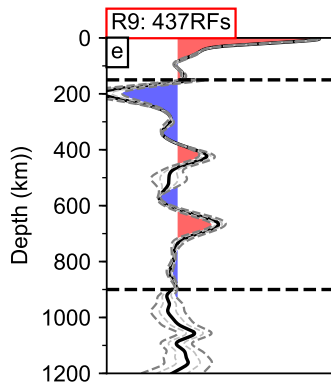
Figure S21. Local depth (*a,c,e*) and slowness stacks (*b,d,f*) for Pds data whose piercing points at 1000 km depth fall within in the specified regions R4, R5, R6. Regions are shown in Figure 7 of the main manuscript. RF max frequency is 0.2 Hz. The number of RFs included in the stack is given in the colored upper left box. High confidence result: green, intermediate: yellow, low confidence: red. Depth stacks comprise RFs corrected to depth using the AFRP20 tomographic model (Boyce et al., 2021). Depth stack amplitudes are multiplied by five and twenty below 150 km and 900 km respectively. Predicted converted Pds arrivals have negative slowness (solid line), multiples have positive slowness (dashed line) w.r.t. direct-P phase. Orange square: d410 conversion/multiple. Green circle: d660 conversion/multiple. Violet triangle: d1000 conversion/multiple.
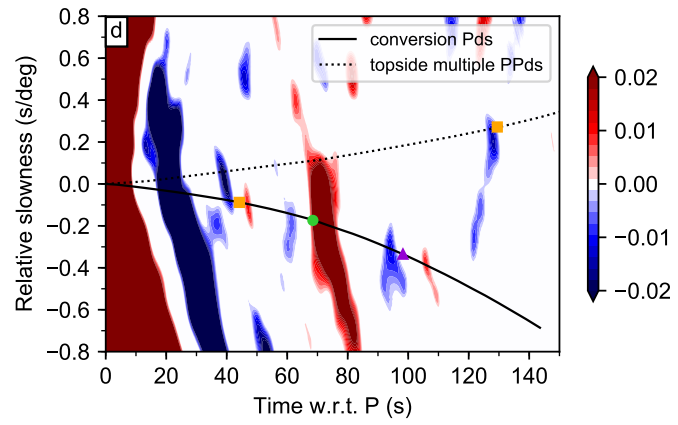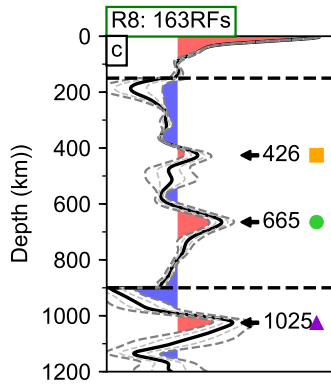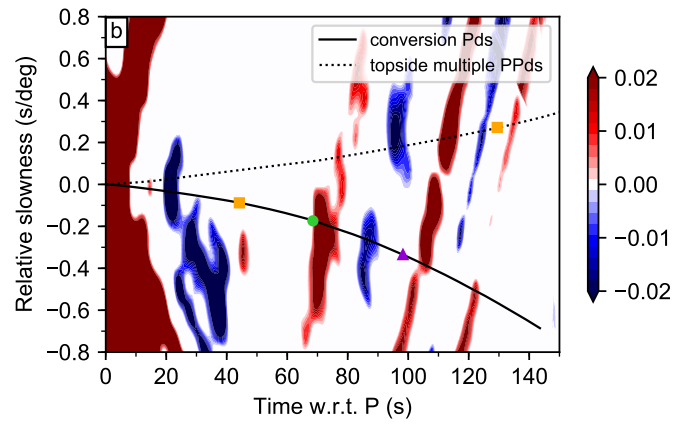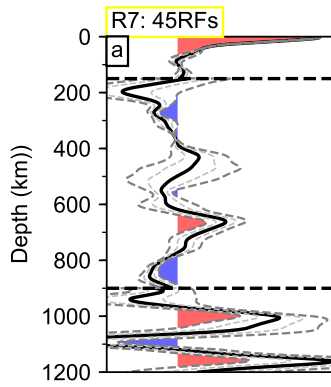
Figure S22.   Local depth (a,c,e) and slowness stacks (b,d,f) for Pds data whose piercing points at 1000 km depth fall within in the specified regions R7, R8, R9. Regions are shown in Figure 7 of the main manuscript. RF max frequency is 0.2 Hz. The number of RFs included in the stack is given in the colored upper left box. High confidence result: green, intermediate: yellow, low confidence: red. Depth stacks comprise RFs corrected to depth using the AFRP20 tomographic model (Boyce et al., 2021). Depth stack amplitudes are multiplied by five and twenty below 150 km and 900 km respectively. The depth of high amplitude peaks at and below MTZ depths are labeled for high confidence stacks. Predicted converted Pds arrivals have negative slowness (solid line), multiples have positive slowness (dashed line) w.r.t. direct-P phase. Orange square: d410 conversion/multiple. Green circle: d660 conversion/multiple. Violet triangle: d1000 conversion/multiple.
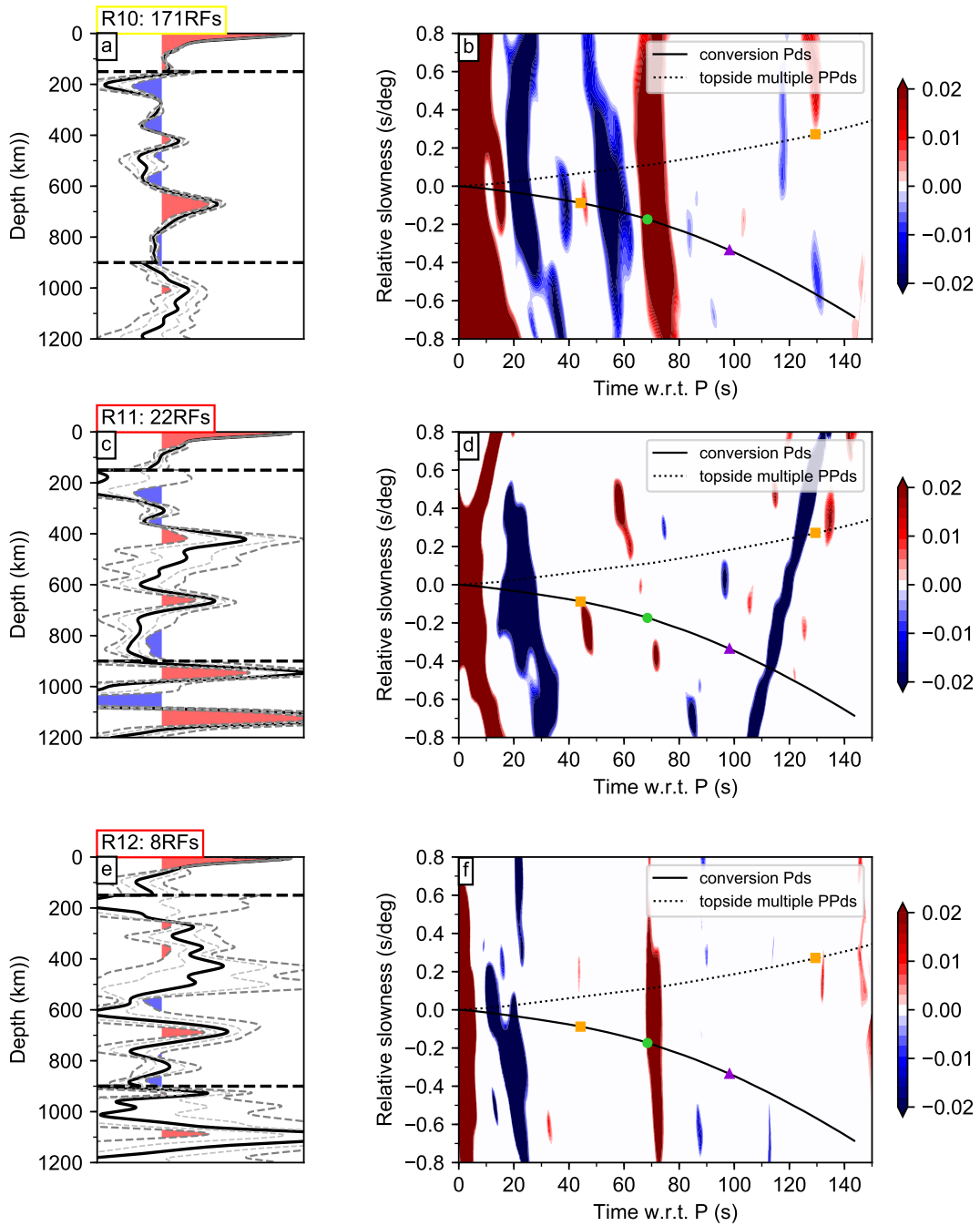
Figure S23. Local depth (a,c,e) and slowness stacks (b,d,f) for Pds data whose piercing points at 1000 km depth fall within in the specified regions R10, R11, R12. Regions are shown in Figure 7 of the main manuscript. RF max frequency is 0.2 Hz. The number of RFs included in the stack is given in the colored upper left box. High confidence result: green, intermediate: yellow, low confidence: red. Depth stacks comprise RFs corrected to depth using the AFRP20 tomographic model (Boyce et al., 2021). Depth stack amplitudes are multiplied by five and twenty below 150 km and 900 km respectively. Predicted converted Pds arrivals have negative slowness (solid line), multiples have positive slowness (dashed line) w.r.t. direct-P phase. Orange square: d410 conversion/multiple. Green circle: d660 conversion/multiple. Violet triangle: d1000 conversion/multiple.
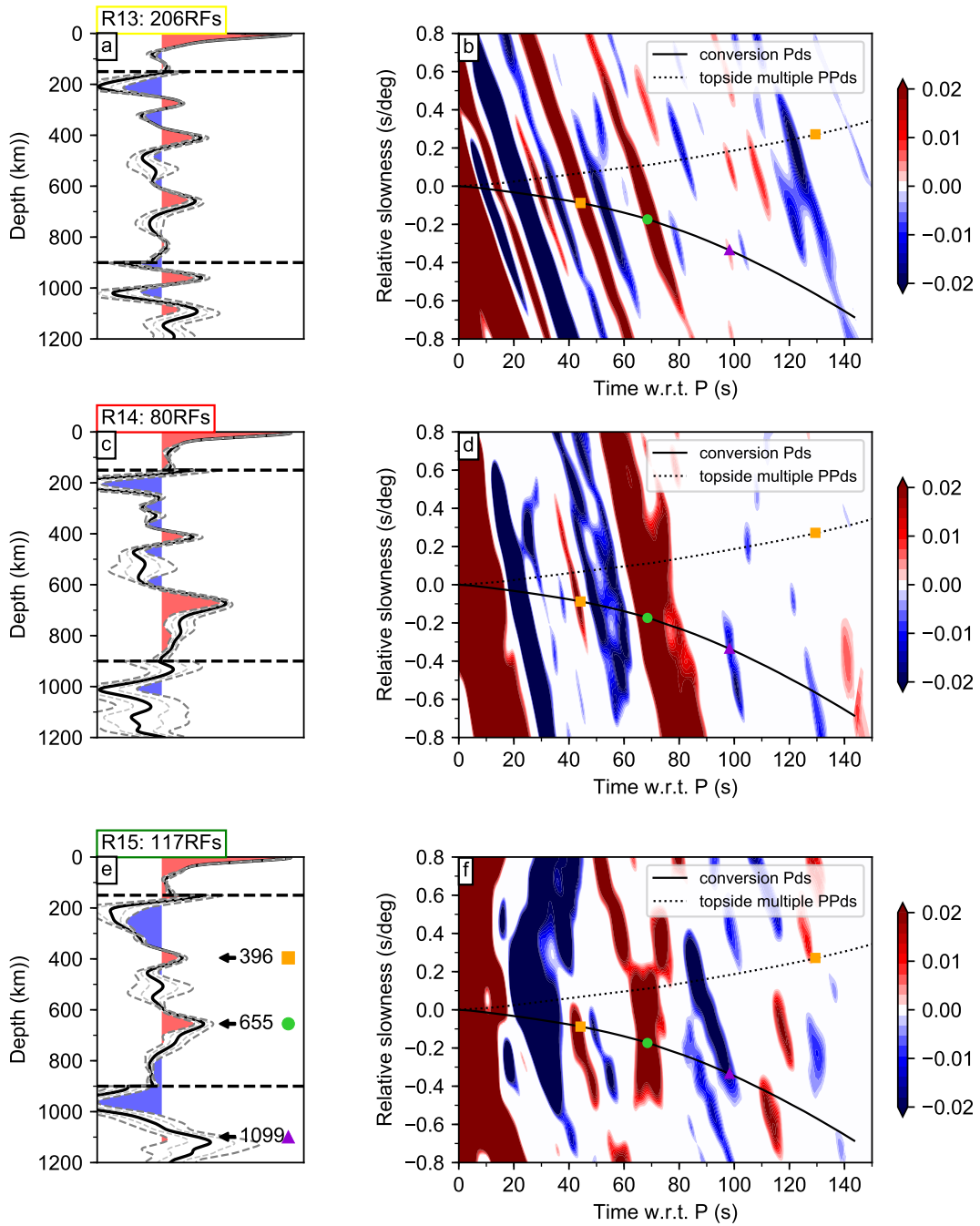
Figure S24. Local depth (a,c,e) and slowness stacks (b,d,f) for Pds data whose piercing points at 1000 km depth fall within in the specified regions R13, R14, R15. Regions are shown in Figure 7 of the main manuscript. RF max frequency is 0.2 Hz. The number of RFs included in the stack is given in the colored upper left box. High confidence result: green, intermediate: yellow, low confidence: red. Depth stacks comprise RFs corrected to depth using the AFRP20 tomographic model (Boyce et al., 2021). Depth stack amplitudes are multiplied by five and twenty below 150 km and 900 km respectively. The depth of high amplitude peaks at and below MTZ depths are labeled for high confidence stacks. Predicted converted Pds arrivals have negative slowness (solid line), multiples have positive slowness (dashed line) w.r.t. direct-P phase. Orange square: d410 conversion/multiple. Green circle: d660 conversion/multiple. Violet triangle: d1000 conversion/multiple.
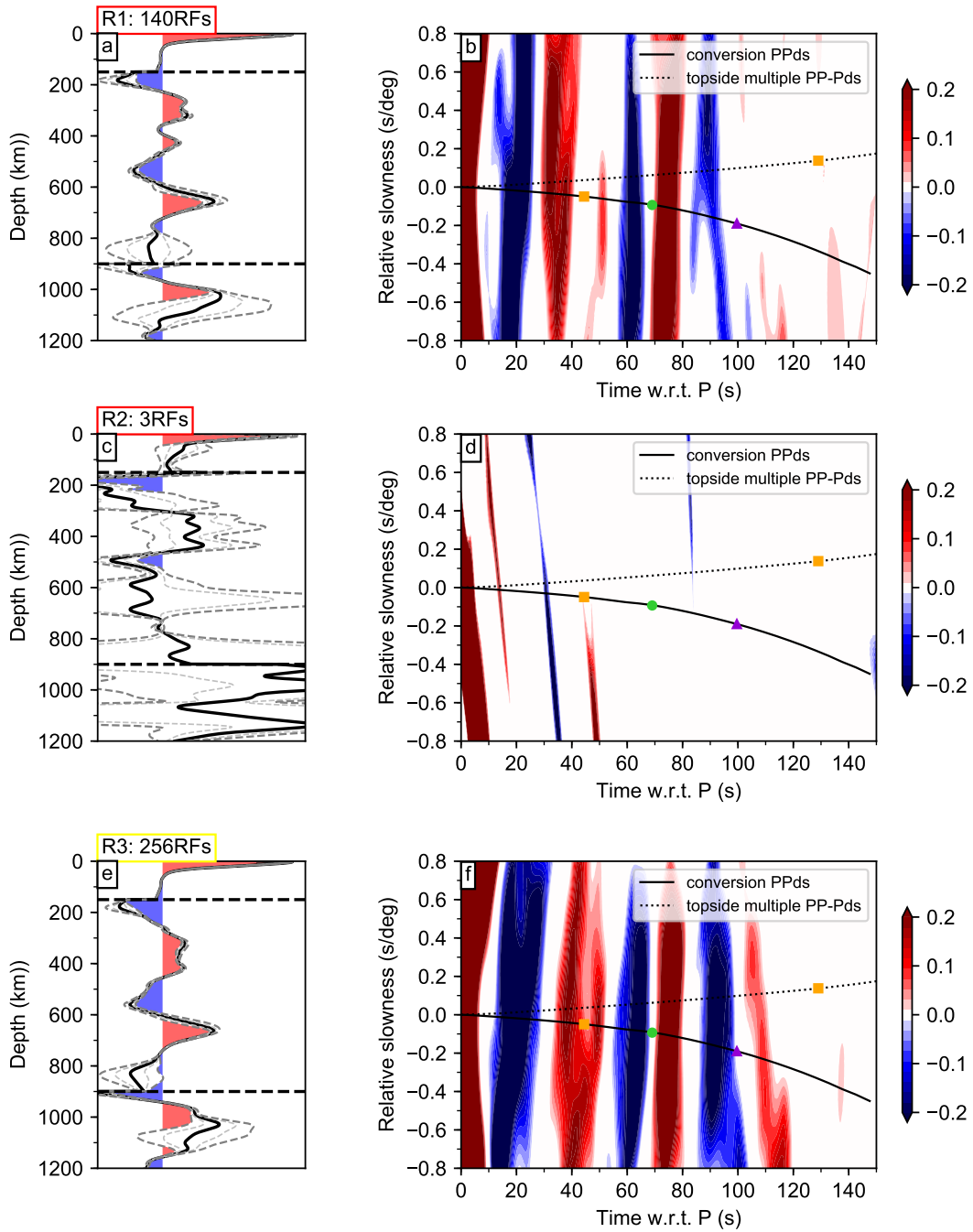
Figure S25. Local depth (a,c,e) and slowness stacks (b,d,f) for PPds data whose piercing points at 1000 km depth fall within in the specified regions R1, R2, R3. Regions are shown in Figure 7 of the main manuscript. RF max frequency is 0.2 Hz. The number of RFs included in the stack is given in the colored upper left box. High confidence result: green, intermediate: yellow, low confidence: red. Depth stacks comprise RFs corrected to depth using the AFRP20 tomographic model (Boyce et al., 2021). Depth stack amplitudes are multiplied by five and twenty below 150 km and 900 km respectively. Predicted converted PPds arrivals have negative slowness (solid line), multiples have positive slowness (dashed line) w.r.t. direct-PP phase. Orange square: d410 conversion/multiple. Green circle: d660 conversion/multiple. Violet triangle: d1000 conversion/multiple.
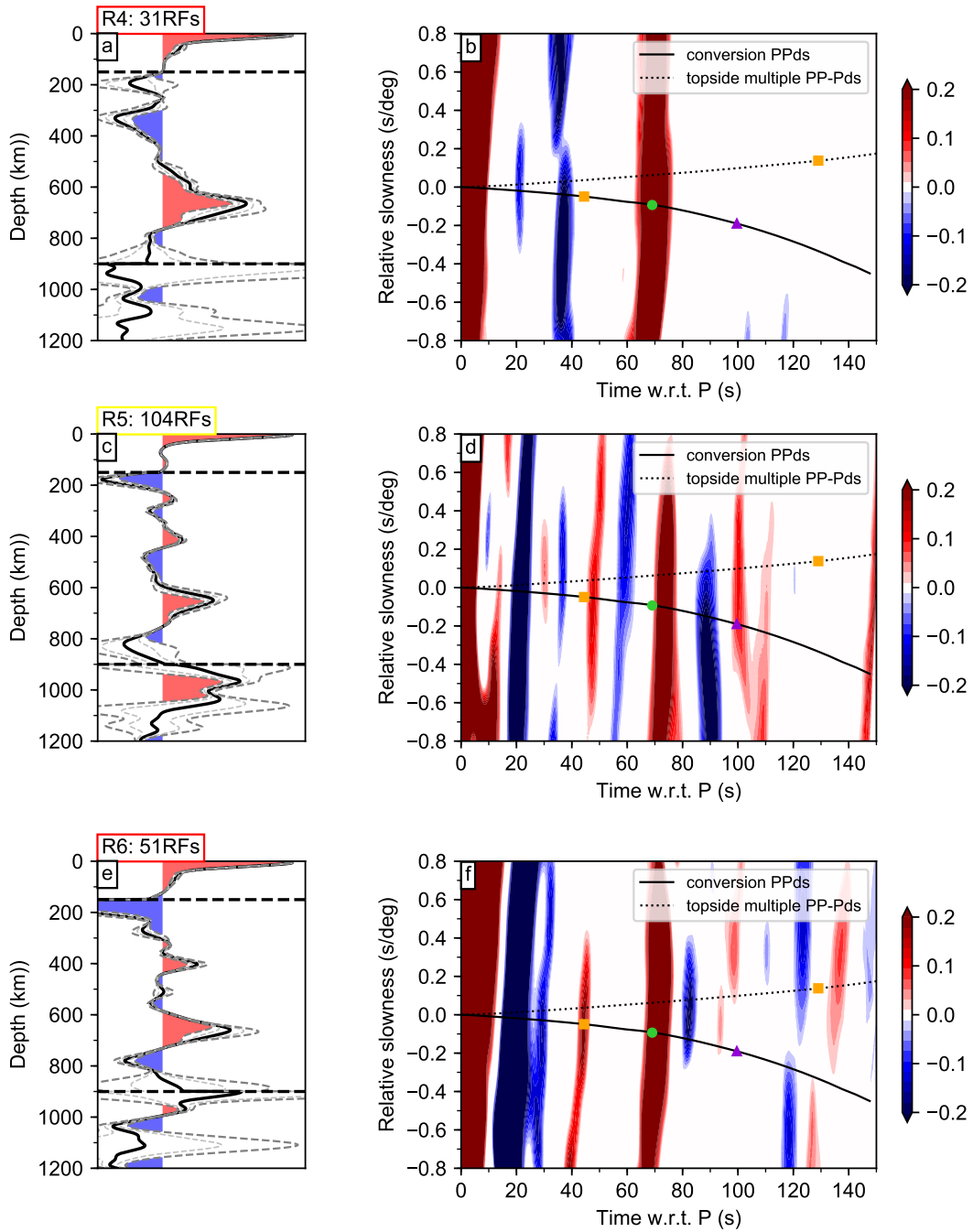
Figure S26. Local depth (*a,c,e*) and slowness stacks (*b,d,f*) for PPds data whose piercing points at 1000 km depth fall within in the specified regions R4, R5, R6. Regions are shown in Figure 7 of the main manuscript. RF max frequency is 0.2 Hz. The number of RFs included in the stack is given in the colored upper left box. High confidence result: green, intermediate: yellow, low confidence: red. Depth stacks comprise RFs corrected to depth using the AFRP20 tomographic model (Boyce et al., 2021). Depth stack amplitudes are multiplied by five and twenty below 150 km and 900 km respectively. Predicted converted PPds arrivals have negative slowness (solid line), multiples have positive slowness (dashed line) w.r.t. direct-PP phase. Orange square: d410 conversion/multiple. Green circle: d660 conversion/multiple. Violet triangle: d1000 conversion/multiple.
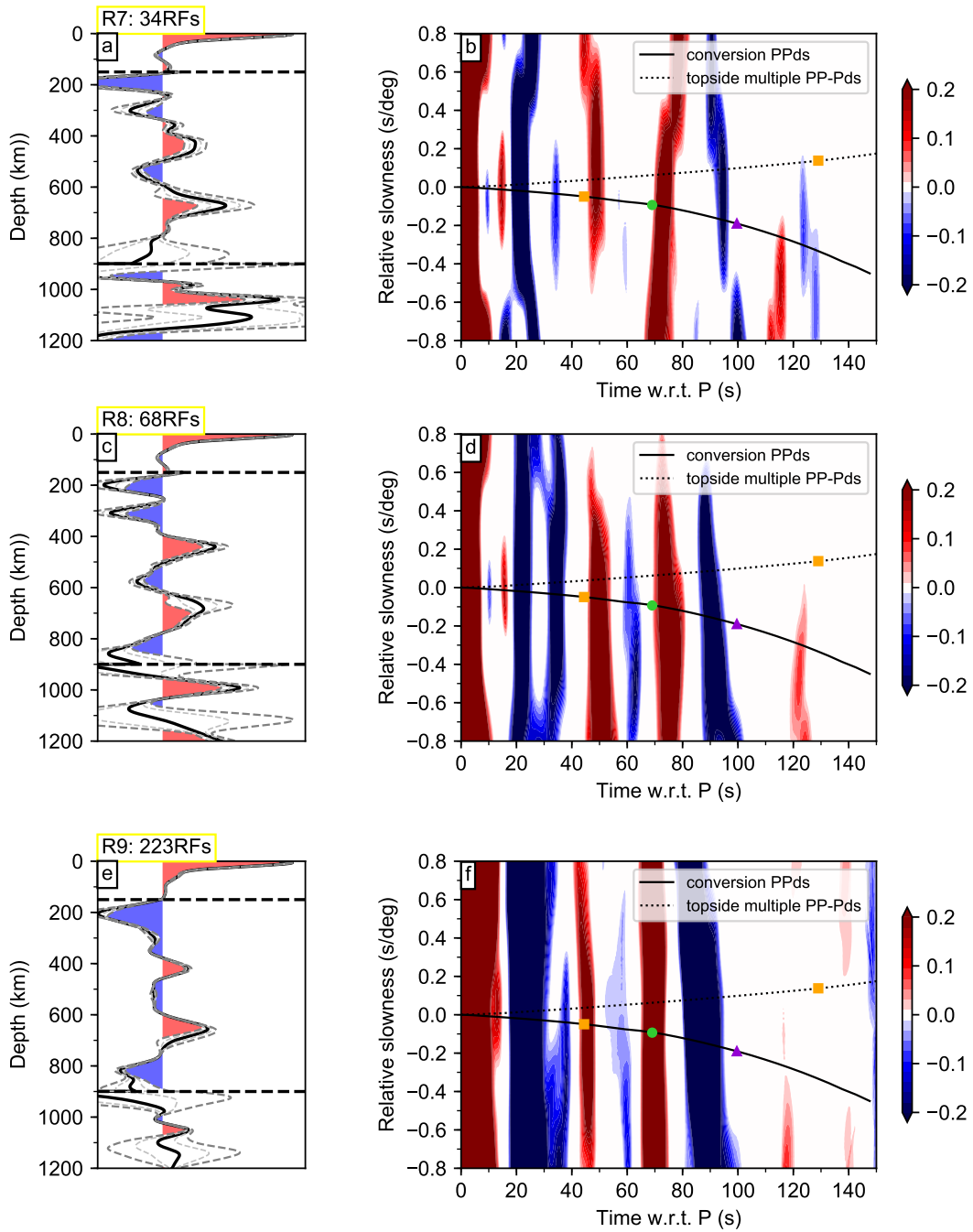
Figure S27. Local depth (a,c,e) and slowness stacks (b,d,f) for PPds data whose piercing points at 1000 km depth fall within in the specified regions R7, R8, R9. Regions are shown in Figure 7 of the main manuscript. RF max frequency is 0.2 Hz. The number of RFs included in the stack is given in the colored upper left box. High confidence result: green, intermediate: yellow, low confidence: red. Depth stacks comprise RFs corrected to depth using the AFRP20 tomographic model (Boyce et al., 2021). Depth stack amplitudes are multiplied by five and twenty below 150 km and 900 km respectively. Predicted converted PPds arrivals have negative slowness (solid line), multiples have positive slowness (dashed line) w.r.t. direct-PP phase. Orange square: d410 conversion/multiple. Green circle: d660 conversion/multiple. Violet triangle: d1000 conversion/multiple.
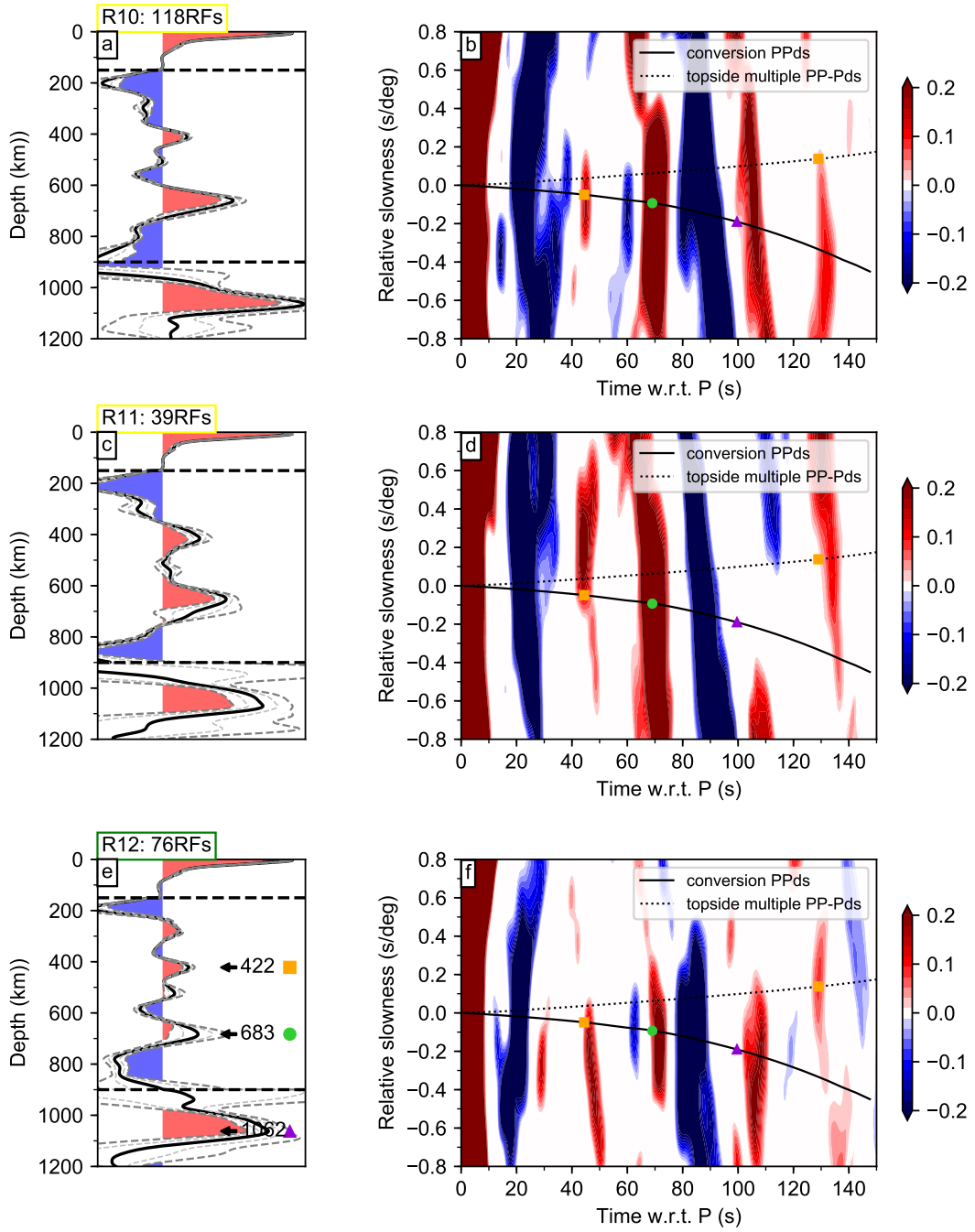
Figure S28. Local depth (a,c,e) and slowness stacks (b,d,f) for PPds data whose piercing points at 1000 km depth fall within in the specified regions R10, R11, R12. Regions are shown in Figure 7 of the main manuscript. RF max frequency is 0.2 Hz. The number of RFs included in the stack is given in the colored upper left box. High confidence result: green, intermediate: yellow, low confidence: red. Depth stacks comprise RFs corrected to depth using the AFRP20 tomographic model (Boyce et al., 2021). Depth stack amplitudes are multiplied by five and twenty below 150 km and 900 km respectively. Predicted converted PPds arrivals have negative slowness (solid line), multiples have positive slowness (dashed line) w.r.t. direct-PP phase. Orange square: d410 conversion/multiple. Green circle: d660 conversion/multiple. Violet triangle: d1000 conversion/multiple.
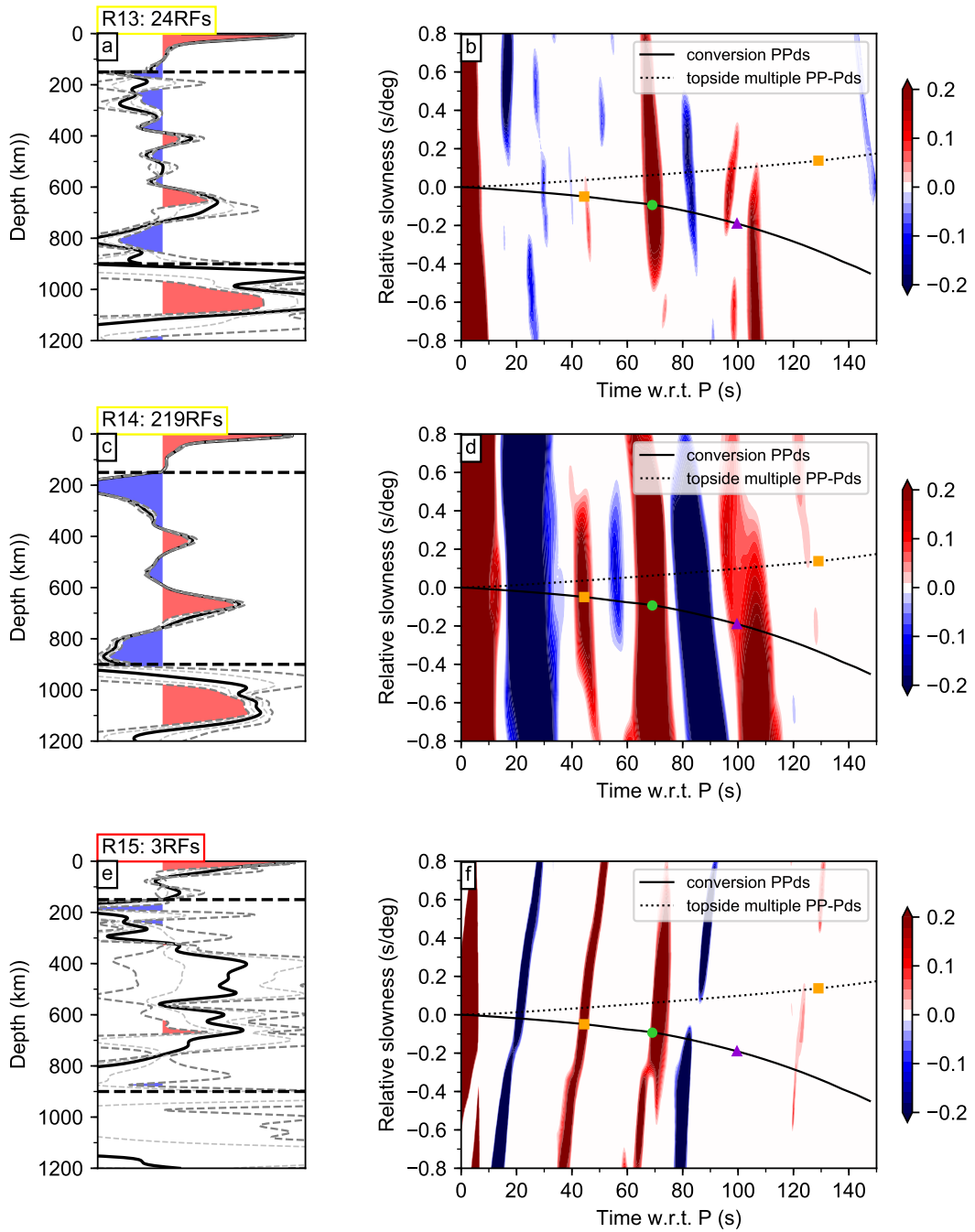
Figure S29. Local depth (a,c,e) and slowness stacks (b,d,f) for PPds data whose piercing points at 1000 km depth fall within in the specified regions R13, R14, R15. Regions are shown in Figure 7 of the main manuscript. RF max frequency is 0.2 Hz. The number of RFs included in the stack is given in the colored upper left box. High confidence result: green, intermediate: yellow, low confidence: red. Depth stacks comprise RFs corrected to depth using the AFRP20 tomographic model (Boyce et al., 2021). Depth stack amplitudes are multiplied by five and twenty below 150 km and 900 km respectively. Predicted converted PPds arrivals have negative slowness (solid line), multiples have positive slowness (dashed line) w.r.t. direct-PP phase. Orange square: d410 conversion/multiple. Green circle: d660 conversion/multiple. Violet triangle: d1000 conversion/multiple.

References

Boyce, A., Bastow, I. D., Cottaar, S., Kounoudis, R., Guilloud De Courbeville, J., Caunt, E., & Desai, S. (2021). AFRP20: New P-wavespeed Model for the African Mantle Reveals Two Whole-Mantle Plumes Below East Africa and Neoproterozoic Modification of the Tanzania Craton. *Geochem. Geophys. Geosyst.*. doi: 10.1029/2020GC009302

Celli, N. L., Lebedev, S., Schaeffer, A. J., & Gaina, C. (2020). African cratonic lithosphere carved by mantle plumes. *Nat. Comms.*, *11*(1), 92. doi: 10.1038/s41467 -019-13871-2

Chang, S. J., Ferreira, A. M. G., Ritsema, J., van Heijst, H. J., & Woodhouse, J. H. (2015). Joint inversion for global isotropic and radially anisotropic mantle structure including crustal thickness perturbations. *J. Geophys. Res.*, *120*(6), 4278–4300. doi: 10.1002/2014jb011824

French, S. W., & Romanowicz, B. (2014). Whole-mantle radially anisotropic shear velocity structure from spectral-element waveform tomography. *Geophys. J. Int.*, *199*(3), 1303–1327. doi: 10.1093/gji/ggu334

Schaeffer, A., & Lebedev, S. (2013). Global shear speed structure of the upper mantle and transition zone. *Geophys. J. Int.*, *194*(1), 417–449. doi: 10.1093/gji/ ggt095

van Stiphout, A. M., Cottaar, S., & Deuss, A. (2019). Receiver function mapping of mantle transition zone discontinuities beneath Alaska using scaled 3-D velocity corrections. *Geophys. J. Int.*, *219*(2), 1432–1446. doi: 10.1093/gji/ggz360